JGR Space Physics

RESEARCH ARTICLE
10.1029/2023JA031363

The Io, Europa, and Ganymede Auroral Footprints at Jupiter in the Ultraviolet: Positions and Equatorial Lead Angles

V. Hue[1,2], G. R. Gladstone[2,3], C. K. Louis[4], T. K. Greathouse[2], B. Bonfond[5], J. R. Szalay[6], A. Moirano[7,8], R. S. Giles[2], J. A. Kammer[2], M. Imai[9], A. Mura[7], M. H. Versteeg[2], G. Clark[10], J.-C. Gérard[5], D. C. Grodent[5], J. Rabia[11], A. H. Sulaiman[12], S. J. Bolton[2], and J. E. P. Connerney[13,14]

[1]Aix-Marseille Université, CNRS, CNES, Institut Origines, LAM, Marseille, France, [2]Southwest Research Institute, San Antonio, TX, USA, [3]University of Texas at San Antonio, San Antonio, TX, USA, [4]School of Cosmic Physics, DIAS Dunsink Observatory, Dublin Institute for Advanced Studies, Dublin, Ireland, [5]STAR Institute, LPAP, Université de Liège, Liège, Belgium, [6]Department of Astrophysical Sciences, Princeton University, Princeton, NJ, USA, [7]Institute for Space Astrophysics and Planetology, National Institute for Astrophysics, Rome, Italy, [8]Sapienza University of Rome, Rome, Italy, [9]Department of Electrical Engineering and Information Science, National Institute of Technology (KOSEN), Niihama College, Niihama, Japan, [10]Johns Hopkins University Applied Physics Laboratory, Laurel, MD, USA, [11]Institut de Recherche en Astrophysique et Planétologie, CNRS-UPS-CNES, Toulouse, France, [12]School of Physics and Astronomy, Minnesota Institute for Astrophysics, University of Minnesota, Minneapolis, MN, USA, [13]NASA Goddard Spaceflight Center, Greenbelt, MD, USA, [14]Space Research Corporation, Annapolis, MD, USA

Key Points:

- Over 1,600 ultraviolet spectral images of the Io, Europa, and Ganymede footprints from Juno are analyzed
- Empirical formulae for the Io, Europa, and Ganymede equatorial lead angles derived from Juno data are provided
- Alfvén travel time estimates are derived, constraining the Alfvénic interaction at the three innermost Galilean moons

Supporting Information:

Supporting Information may be found in the online version of this article.

Correspondence to:

V. Hue,
vincent.hue@lam.fr

Citation:

Hue, V., Gladstone, G. R., Louis, C. K., Greathouse, T. K., Bonfond, B., Szalay, J. R., et al. (2023). The Io, Europa, and Ganymede auroral footprints at Jupiter in the ultraviolet: Positions and equatorial lead angles. *Journal of Geophysical Research: Space Physics*, *128*, e2023JA031363. https://doi.org/10.1029/2023JA031363

Received 1 FEB 2023
Accepted 20 APR 2023

Abstract Jupiter's satellite auroral footprints are a consequence of the interaction between the Jovian magnetic field with co-rotating iogenic plasma and the Galilean moons. The disturbances created near the moons propagate as Alfvén waves along the magnetic field lines. The position of the moons is therefore "Alfvénically" connected to their respective auroral footprint. The angular separation from the instantaneous magnetic footprint can be estimated by the so-called lead angle. That lead angle varies periodically as a function of orbital longitude, since the time for the Alfvén waves to reach the Jovian ionosphere varies accordingly. Using spectral images of the Main Alfvén Wing auroral spots collected by Juno-UVS during the first 43 orbits, this work provides the first empirical model of the Io, Europa, and Ganymede equatorial lead angles for the northern and southern hemispheres. Alfvén travel times between the three innermost Galilean moons to Jupiter's northern and southern hemispheres are estimated from the lead angle measurements. We also demonstrate the accuracy of the mapping from the Juno magnetic field reference model (JRM33) at the completion of the prime mission for M-shells extending to at least 15 R_J. Finally, we shows how the added knowledge of the lead angle can improve the interpretation of the moon-induced decametric emissions.

Plain Language Summary The interaction between the Jovian magnetospheric plasma and the Galilean moons gives rise to a complex set of phenomena, including the generation of auroral spots magnetically related to the moons and the generation of radio emissions. The magnetic perturbations local to the moons propagate at a finite speed along the magnetic field lines, and reach the northern and southern Jovian hemispheres where they produce the auroral spots. Studying the position of these auroral spots and how they vary over a complete Jovian rotation provides information about the magnetic mapping, as they map directly to the actual physical positions of the moons. The magnetic field model derived from Juno's prime mission is in good agreement with the observation of the satellite footprints. This paper provides information about how the electromagnetic perturbation resulting from the interaction propagates at a finite speed to create auroral spots, leading to an angular shift between the instantaneously magnetically-mapped position of the moon and the auroral footprint, a quantity also known as the "equatorial lead angle". The present work provides an empirical fit of the equatorial lead angle for Io, Europa, and Ganymede derived from Juno data.

1. Introduction

Jupiter's volcanically-active moon Io is a major source of plasma within the Jovian magnetosphere. Over a ton per second of sulfur dioxide escapes from the moon as a neutral cloud around the moon. High-energy electrons trapped in Jupiter's magnetosphere dissociate and ionize the neutral material, producing ions which get picked up by Jupiter's strong rotating magnetic field, forming the Io plasma torus. The plasma is then radially transported outwards over the timescale of several weeks as a plasma sheet with a typical scale height of about 1 R_J (1

$R_J = 71{,}492$ km), and confined around the centrifugal equator, near the magnetic equator, that is, the points along the magnetic field lines that are farthest from the spin axis of Jupiter (e.g., Acuna et al., 1983; Belcher, 1983).

Evidence of the magnetospheric interaction at Io was discovered early on through the detection of decametric radio emission (Bigg, 1964). The subsequent Voyager 1 measurements near Io led to formalize the interaction model at the moon resulting in the generation of an Alfvénic disturbance (Acuna et al., 1981; Belcher et al., 1981; Goldreich & Lynden-Bell, 1969; Neubauer, 1980). These Alfvén waves propagate to Jupiter along the magnetic field lines toward both polar regions, and their multiple reflections off of the plasma density gradients along the way were later proposed to be responsible for the multiple Io-controlled decametric radio arcs observed (Gurnett & Goertz, 1981).

When the Alfvénic perturbations reach high Jovian latitudes, they accelerate electrons toward and away from Jupiter, as well as protons, leading to the generation of the auroral footprints and decametric radio waves (Hess, Delamere, et al., 2010; Szalay, Bagenal, et al., 2020), which were initially detected in the infrared (IR) and later in the ultraviolet (UV) (Clarke et al., 1996; Connerney et al., 1993; Prangé et al., 1996). Detection of the Europa, and Ganymede auroral footprints using the Hubble Space Telescope (HST) followed shortly after (Clarke et al., 2002).

The overall strength of the moon-magnetosphere interaction depends on the magnetic field strength, the plasma density, the conductivity, as well as the electron acceleration efficiency (Saur et al., 2013; Sulaiman et al., 2023). Because Jupiter's magnetic dipole is tilted from its spin axis by about 10°, the plasma sheet sweeps through the Galilean moons twice every ∼10 hr-rotation period. In the reference frame centered about the plasma sheet, the moons travel up and down the sheet, experiencing denser plasma condition at its the center. The multiple reflections of the Alfvén waves on Alfvén speed gradients, such as near the ionosphere, create multiple auroral spots, whose relative position, morphology, and distribution is modulated by the moon centrifugal latitude, as reported by remote sensing observations (e.g., Bonfond et al., 2008; Mura et al., 2018).

Extensive campaigns using the HST have allowed categorizing the variable morphology of the Io footprints structure as a function of the location of Io with respect to the plasma sheet (Bonfond et al., 2008; Gérard et al., 2006; Wannawichian et al., 2013). These studies showed that the Main Alfvén Wing (MAW) spot was sometimes preceded by a leading spot, named the Transhemispheric Electron Beam (TEB) spot, for a very specific range of sub-Io Jovian longitudes. In that case, the Alfvén waves generated in the wing of the interaction region later reached Jupiter's ionosphere. This means the beam of electrons generating the TEB spot was accelerated anti-planetward by the MAW on the opposite hemisphere, then traveled along the magnetic field line throughout the torus, unaffected by the higher plasma torus density there (Bonfond et al., 2008; Hess et al., 2013).

The Juno mission has brought a wealth of new observations that significantly enhanced our understanding of the moon-magnetosphere interaction (Bolton et al., 2017; Connerney et al., 2017). Juno crosses the magnetic shells connected to the orbits of Io, Europa, and Ganymede at least twice per orbit. Not only did Juno measure the field and particles within the magnetic fluxtube connected to the discrete auroral footprint spots or tail, but it also provided unprecedented infrared and ultraviolet observations both at the highest spatial resolution ever achieved (Mura et al., 2018), and with viewing geometries not accessible from HST (Hue, Greathouse, et al., 2019).

Prior to Juno, there was a debate regarding the processes responsible for the footprint tail emission. One set of studies favored a quasi-steady current system transferring angular momentum from the Jovian ionosphere to the sub-corotating plasma in the moon wakes, and which would be characterized by beams of electron discrete in energies (e.g., Delamere et al., 2003; Goldreich & Lynden-Bell, 1969; Hill & Vasylinas, 2002; Su et al., 2003). Other studies suggested it results from the multiple bouncing of the Alfvén waves generated at the moons, which would be characterized by bidirectional electron populations with broadband energy distributions (e.g., Bonfond et al., 2009; Bonfond, Saur, et al., 2017; Crary & Bagenal, 1997; Hess, Delamere, et al., 2010; Jacobsen et al., 2007).

Early Juno measurements demonstrated the Alfvénic nature of the interaction associated with the Io footprint tail (Damiano et al., 2019; Gershman et al., 2019; Sulaiman et al., 2020, 2023; Szalay, Allegrini, et al., 2020b; Szalay et al., 2018). Szalay et al. (2018); Szalay, Allegrini, et al. (2020b) showed that the electron energy flux, obtained by the multiple Juno-JADE measurements along the Io footprint tail, is a function of the angular separation along Io's orbit between the moon and the MAW spot tracked from Jupiter's ionosphere to the satellite orbit. This angle is also known as “Io-Alfvén tail distance”. Juno measured upward ion conics, that is, protons with angular distribution concentrated along the loss-cone, detected simultaneously with ion cyclotron waves, showing that energetic ions are also generated from moon-magnetosphere interaction (Clark et al., 2020), as well as low-energy

ion acceleration in the vicinity of the MAW, both near the ionosphere and near the Io torus boundary (Szalay, Bagenal, et al., 2020). Additionally, the cyclotron maser instability (CMI) driven by a loss-cone distribution has been established as a major process at Jupiter in generating hectometric and decametric emissions, induced or not by the Galilean moons (Louarn et al., 2017; Louarn et al., 2018; Louis et al., 2020).

Alfvénic acceleration processes were also observed when crossing the fluxtube connected to Ganymede's footprint tail (Szalay, Allegrini, et al., 2020a). One particular Ganymede fluxtube crossing (on PJ30, 8 November, 2020), during which Juno was connected for the first time to the leading-most Ganymede auroral spot, brought a set of in-situ and remote sensing measurements consistent with what was expected during a TEB crossing (Hue et al., 2022). Unlike for Io and Ganymede, crossing through the fluxtube connected to the Europa footprint tail showed signs of electron distribution resulting at least in part from electrostatic acceleration processes (Allegrini et al., 2020). Whether this is a fundamental difference of the interaction at Europa, or that it actually also corresponded to a TEB crossing remains to be ascertained by additional studies of the Europa footprint tail crossings. Radio emissions are also observed associated with Ganymede's interaction (Louis et al., 2020).

The scope of this paper is to process the ultraviolet auroral footprint observations performed from the first perijove (PJ, hereafter) on 8 August 2016 until PJ43 (5 July 2022) with the ultraviolet spectrograph on Juno (Juno-UVS). Section 2 describes the observations and data reduction procedure. In Section 3, the reported satellite footprint locations are compared against the predicted satellite footpaths from the magnetic field model JRM33 (Connerney et al., 2022). From the position of the MAW spot of the satellites, the equatorial lead angle can be estimated using a magnetic field model. The equatorial lead angle is the angular shift, calculated along the orbital motion of the moons, between the actual position of the moons and the position of the MAW footprint mapped instantaneously to the orbital plane of the moon. We then calculate the equatorial lead angles for Io, Europa and Ganymede and provide an empirical fit on Section 4, as well as estimates of the Alfvén travel times for each of the three moons. We subsequently discuss the lead angle variation measured in Section 5. Finally, in Section 6, we present an additional example on the use of the lead angle for the interpretation of the Ganymede-induced decametric emission.

2. Juno-UVS Observations

Juno is a spin-stabilized spacecraft placed in a polar and highly eccentric orbit around Jupiter since July 2016 (Bolton et al., 2017). Each orbit, Juno performs a close flyby of the northern polar region first, reaches closest approach at lower Jovian latitudes at an altitude of about 4,000 km, and then flies above the southern polar region. Because Juno's orbit is highly elliptical and because its closest approach velocity with respect to Jupiter is about 58 km/s, it takes Juno about 2 hours to fly from north to south pole. This implies that the spatial resolution of the remote sensing instrument such as UVS varies drastically over the course of a perijove observation sequence. As the mission is progressing, the orbital period, which was initially around 53 days, was reduced to a shorter orbit, and will be reduced down to 33 days around PJ75 (15 August 2025). Each major orbital period reduction follows a Galilean moon flyby. Juno's orbit precesses over time and the sub-spacecraft PJ latitude increases as the mission continues. The viewing window of UVS over the northern and southern auroras grows increasingly more asymmetric with the mission, with the viewing window of the northern aurora decreasing over time.

Some of the magnetospheric goals of Juno include performing in-situ measurements of the particle population in Jupiter's magnetosphere using an electron and ion sensors suite, while remotely sensing the associated infrared and ultraviolet aurora they may trigger on Jupiter or on the Galilean moons (Bagenal et al., 2017). The Ultraviolet Spectrograph (UVS) is a photon-counting imaging spectrograph operating in the 68–210 nm range (Gladstone et al., 2017). Each spin of Juno, UVS records a swath of UV emission along its 7.2°-long slit, with a typical point-source integration time of 17 ms. The point-spread function (PSF) and spectral resolution are respectively 0.1° and 1.3 nm, at best (Davis et al., 2011; Greathouse et al., 2013), meaning that UVS can resolve features on Jupiter down to 60 km at PJ. Because Juno is flying above both auroral regions at higher altitude, UVS can rather resolve features in the ∼150–400 km range there. Counts recorded on the detector are then converted into brightness using the instrument effective area derived from thousands of stellar observations recorded throughout the mission in between PJ observation sequences (Hue et al., 2021; Hue, Gladstone, et al., 2019).

UVS is equipped with a scan mirror that allows its field of regard to be shifted up to ±30° away from the spin plane. Juno's spinning nature combined with UVS' mirror pointing capability allows building up complete maps of Jupiter's aurora by co-adding consecutive swaths of data. The best temporal resolution of UVS is constrained by the spin rate of Juno and cannot be less than 30 s.

The satellite auroral footprints represent a direct magnetic mapping to a given orbital distance, through the prism of the sub-Alfvénic interaction around each moon. It is worth differentiating at this point magnetic mapping from Alfvénic mapping. The MAW spot is Alfvénically connected to the physical position of the moon, which differs from the instantaneous field-line tracing magnetically connecting the moon and Jupiter's ionosphere. Because of the Jovian rotation and the moon orbital motion, there is a displacement of the satellite footprints location between two consecutive UVS images recorded 30 s apart, which can be estimated considering each moon's synodic period:

$$P_{moon}^{syn} = \frac{P_{Jup}\, P_{moon}}{P_{moon} - P_{Jup}}, \tag{1}$$

where P_{Jup} and P_{moon} are respectively the rotation period of Jupiter and orbital periods of a moon. Relationship (1) leads to $P_{io}^{syn} = 12.89$ hr; $P_{europa}^{syn} = 11.22$ hr; $P_{ganymede}^{syn} = 10.53$ hr. Over the course of a Juno spin (~30 s), the moon spans a longitudinal sector of $\Delta\lambda_{moon} = \left(360/P_{moon}^{syn}\right) \times 30$, where P_{moon}^{syn} is in seconds. This leads to $\Delta\lambda_{io} = 0.23°$; $\Delta\lambda_{europa} = 0.27°$; $\Delta\lambda_{ganymede} = 0.28°$ between two consecutive swaths. Over one Juno spin and using the JRM33 model, this leads to a displacement of the instantaneous field line from the moon to Jupiter's northern ionosphere up to 223 km, 220 km, and 191 km, respectively for Io, Europa, and Ganymede. In the south, that same smearing ranges up to 141 km, 136 km, and 114 km for Io, Europa, and Ganymede, respectively. Note that all longitudes (λ) quoted in this work are west longitudes in System III reference frame, and are calculated according to the 1965 system three rotation period (Dessler, 1983).

In order to increase the signal-to-noise ratio (SNR), without smearing the signal of the satellite footprint emission, the choice was made to bin the UVS data by two consecutive spins worth of data. Various auroral emissions may be present close to the footprints, such as emission from the main oval (Bonfond et al., 2021; Ebert et al., 2021), injection signatures (e.g., Bonfond, Gladstone, et al., 2017), or increased background radiation (Bonfond et al., 2018; Kammer et al., 2019). The change of geometry, background emission and SNR makes challenging extracting the precise location of the footprints, particularly for the Europa, and Ganymede footprints, generally located rather close to the main oval emission and auroral injections. For these reasons, the footprint locations were manually extracted by visual inspection of consecutive series of two spins-averaged UVS data. Since the moons are not in co-rotation with Jupiter, identifying the satellite footprints over consecutive spins worth of data is achieved by visually inspecting auroral spots that are in sub-corotation around a background of mostly corotating auroral emission. Figure 1 shows an example of consecutive 2-spin averaged spectral image recorded by UVS of the Io, Europa, and Ganymede footprints.

The uncertainties in the derived location of the different observed footprints were calculated as the quadratic combination of the uncertainty due to the instrument point-spread-function (PSF), and the uncertainty due to the projected scale height H of the footprint emission curtain. While the former uncertainty only depends on the distance between Juno and the footprint of interest, the latter depends on the footprint emission angle as seen by Juno. The uncertainties on the footprint longitude (λ), latitude (ϕ) therefore reads:

$$\sigma_{\lambda,\phi}^2 = \sigma_{PSF}^2 + \sigma_{P\,\lambda,\phi}^2, \tag{2}$$

where σ_{PSF} is calculated as the projection of the ~0.1° UVS PSF along the latitude and longitude grid. $\sigma_{P\,\lambda,\phi}$ is calculated as the projected extent of the footprint emission curtain, H, as illustrated on Figure 2, assuming as a first approximation that the auroral curtain is vertical. P is given as $P = H/\tan\beta$, and $\beta = \pi/2 - e - \epsilon$, where e (emission angle) and ϵ are angles calculated using NAIF's SPICE kernels (C. H. Acton, 1996; C. Acton et al., 2018). H was taken as 366 km, that is, the typical scale height of a Chapman profile derived from Io's MAW spot by Bonfond (2010).

Only the data recorded by UVS when Juno was 1.5 hr about perijove was used, that is, when the ~0.1° PSF projected at 45° on Jupiter's surface was lower than the typical width of the footprints as previously derived from HST (Bonfond, 2010). From PJ1 until PJ43, this results in a set of 211 (Io), 108 (Europa) and 160 (Ganymede) 2-spin averaged UVS images in the north, and 585, 264 and 299 in the south for Io, Europa, and Ganymede, respectively. The projection altitude of the UV data on Jupiter used for this work was 900 km above the 1-bar level, after Bonfond (2010); Szalay et al. (2018).

3. Satellite Footprint Locations

Measuring accurately the location of the satellite footprint emission gives a precise magnetic mapping of the orbital position of the moons. Comparing the observed footprint position of, for example, Io, against the predicted magnetic mapping of that moon gives an estimate of the mapping accuracy. Earlier magnetic field models of

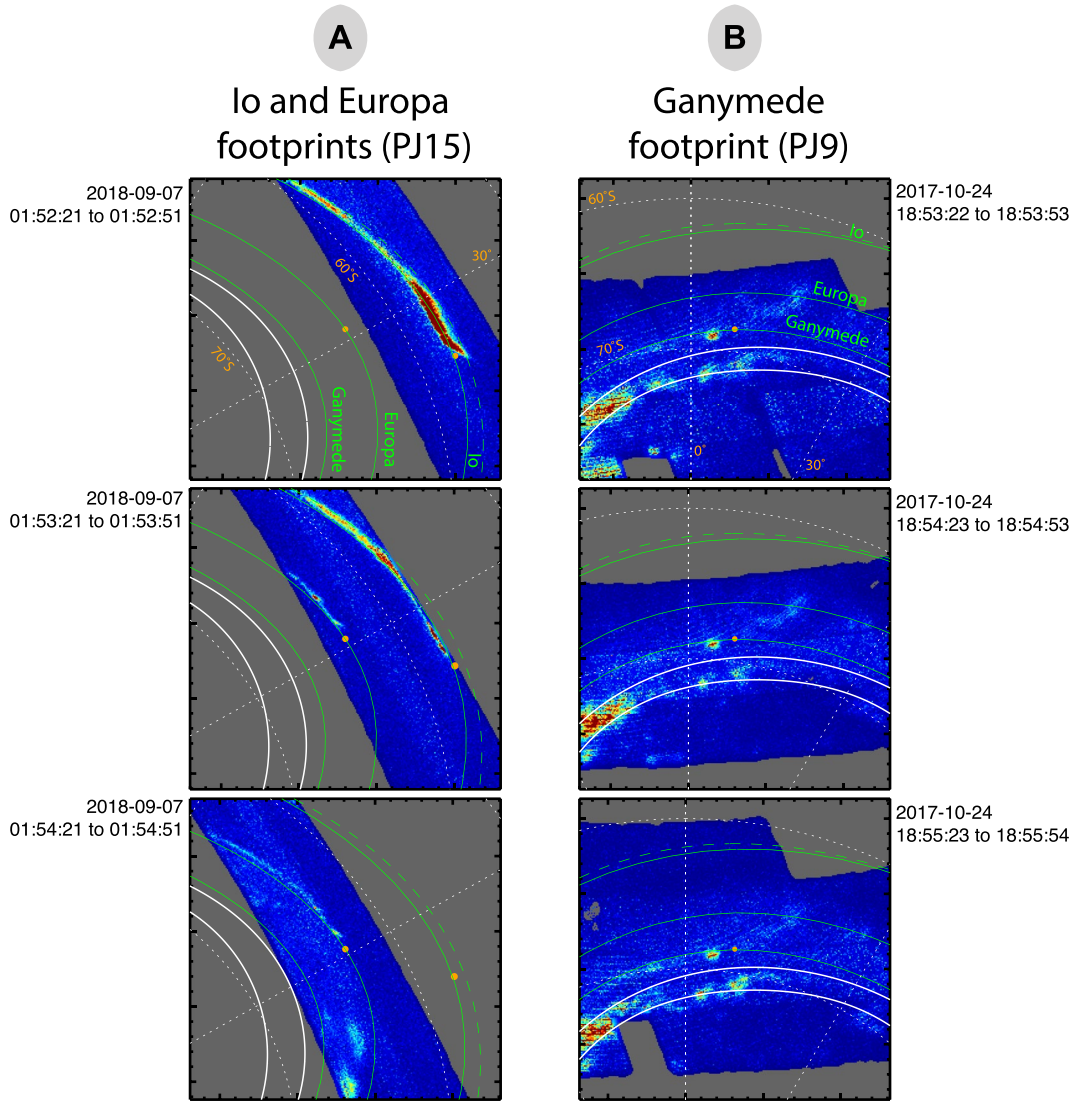

Figure 1. 2-spin averaged Juno-UVS spectral images of the Io and Europa footprints (panel A), and the Ganymede footprints (panel B) over the southern hemisphere. The UVS nadir time of the two consecutive spins are listed as UTC time. The instantaneous moon magnetic footprint positions according to the JRM33 model is shown as orange dots along the satellite footprints, also calculated using JRM33 and shown as solid green line. The satellite footpath of Io from Bonfond, Saur, et al. (2017) is shown as dashed green lines. The solid white lines show the reference location where the main oval is observed (Bonfond et al., 2012).

Jupiter were constructed using in-situ spacecraft measurements as well as the Io footprint location derived from IR and UV observations. This initially allowed Connerney et al. (1998) to constrain the VIP4 model, using observations of the Io footprints in the IR. When employing a larger set of Io footprint observations obtained in the UV, the method was extended by Hess et al. (2011) to produce the VIPAL magnetic field model. That model additionally included the longitudinal constraint on the Io footprint location, which originates from the finite Alfvén travel time between the interaction region near the moon to Jupiter's ionosphere. Later, Hess et al. (2017) further constrained Jupiter's magnetic field model by adding also Europa's and Ganymede's auroral footprint locations to produce the ISaAC magnetic field model.

The position of the Io, Europa, and Ganymede footprints are presented in Figure 3, and are plotted against the satellite footpath contours predicted from the JRM33 model (Connerney et al., 2022), combined with the Juno-era current sheet model (Connerney et al., 2020). Unlike the HST observations, UVS observed the footprints from a wide range of emission angles (*e* on Figure 2) from 1° to 77°, as well as from a wide range of altitude, from 0.3 R_J to 2.6 R_J.

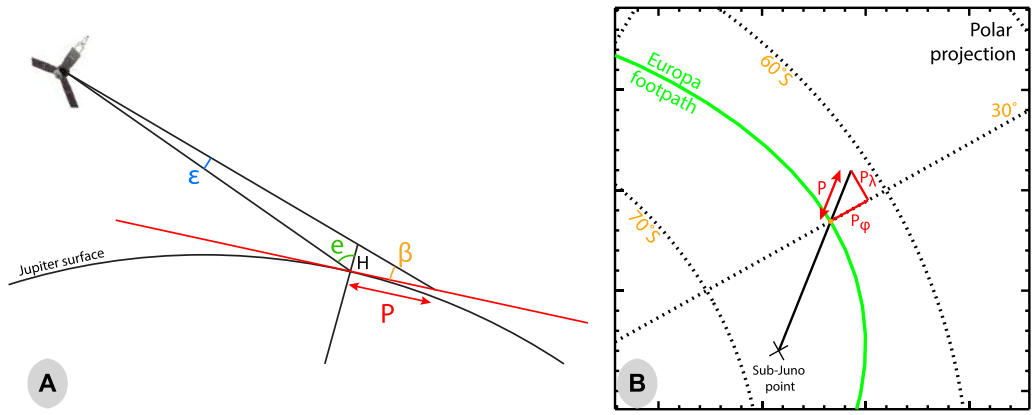

Figure 2. Uncertainty calculation on the derived latitude and longitude of the footprints. Panel (a) calculation of the projected height of a typical auroral footprint vertical emission P along the Juno line of sight. The latitude and longitude uncertainty (P_ϕ, P_λ) are calculated through the decomposition of P, exaggerated here for illustration purposes, along the latitude and longitude grid (panel B). e is the emission angle, while β and ϵ are two angles used to calculate the projection of P.

Because of the precession of Juno's orbit, Juno-UVS gets an increasingly shorter look over the northern aurora as the mission progresses. This causes a greater density of footprint position measurements in the south, despite the rapid increase of Juno's altitude over the south pole during the outbound leg. The magnetic field model obtained after the completion of the prime mission (JRM33) predicts a magnetic footpath for the satellite in very good agreement with the Juno-UVS observations (Connerney et al., 2022). One region which previously showed significant differences between the observed and predicted satellite footprint location is the auroral kink

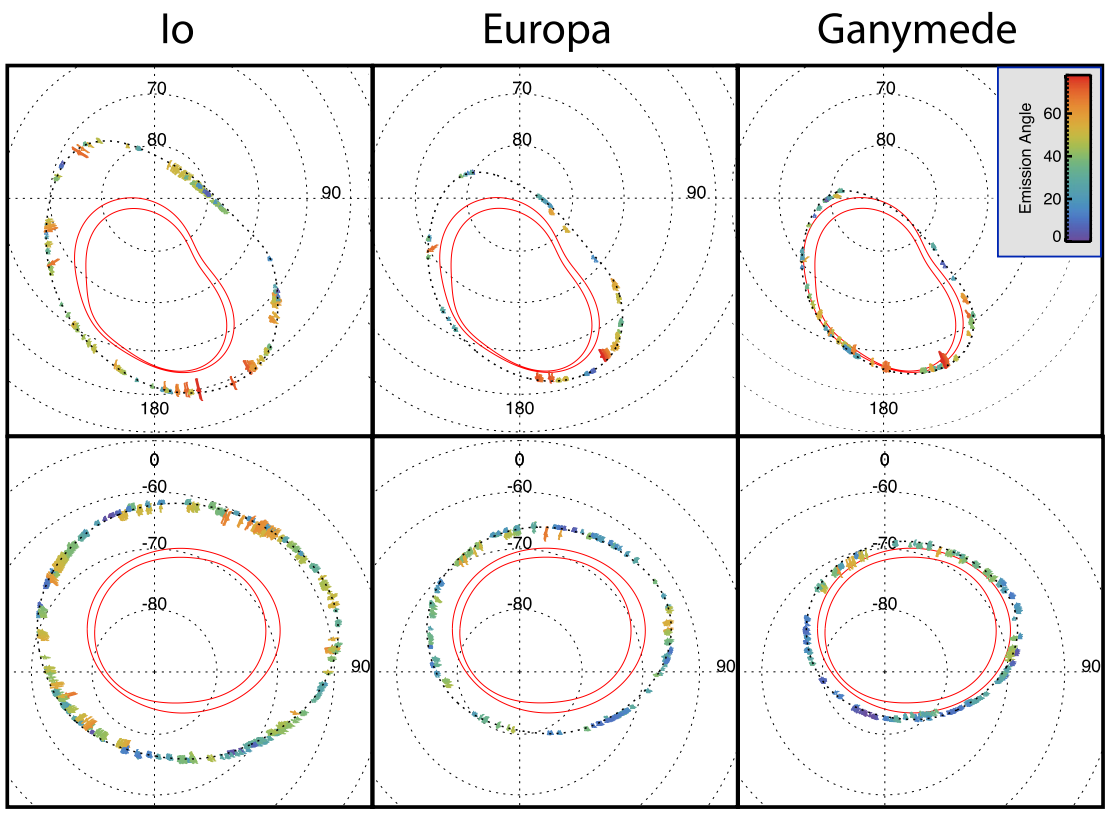

Figure 3. Extracted position of the Io, Europa, and Ganymede Main Alfvén Wing footprints in the north (top panels) and south (bottom panels), using Juno-UVS data recorded from perijoves 1 to 43 and color-coded according to the emission angle observed by Juno-UVS. The solid red lines show the reference oval from Bonfond et al. (2012). The black dotted line show the satellite footpaths as predicted from the JRM33 model (Connerney et al., 2022).

sector, at longitudes from 80° to 150° in the northern hemisphere only, for which Grodent et al. (2008) suggested the inclusion of a magnetic anomaly to the existing magnetic field model at that time, in order to better fit the footprint location. Early Juno measurements for instance showed significant differences between the predicted Europa footprint location in that sector, and the observed one (Allegrini et al., 2020). JRM33 is now in very good agreement with the observed MAW spot positions in that sector for all 3 inner Galilean moons.

Despite the more extended UVS coverage than HST in the south, there are several longitude gaps in the northern MAW observation not covered by Juno-UVS as of PJ43. For the northern Io MAW spot, there are gaps at footprint longitudinal sectors of 260°–280°; 100°–118°; 342°–20°. For the northern Europa MAW, the gaps are 300°–80°; 175°–206°; 215°–238°; 250°–290°. For the northern Ganymede MAW, the main longitude gap is 280°–130°. The MAW footprint latitude/longitude locations for Io, Europa, and Ganymede are provided in Supporting Information S1. The difference in coverage with previous HST observations can be compared with Figures 1 and 2 showed in Supporting Information of Bonfond, Saur, et al. (2017).

By binning the measured MAW positions over 1.5°-wide longitudinal sector to minimize the measurements scattering, and only considering the MAW spot position recorded at emission angles lower than 20°, one can assess the accuracy of magnetic field models, such as JRM33, while limiting the uncertainty resulting from the range of viewing geometries. For Io, the average distance between the JRM33-computed reference footpath and the observed MAW positions is 511 ± 28 km in the north and 274 ± 64 km in the south. For Europa, these numbers are 141 ± 26 km in the north and 322 ± 61 km in the south. For Ganymede, these numbers are 213 ± 44 km in the north and 343 ± 64 km in the south. These numbers provide an order-of-magnitude estimate in mapping uncertainty between the model and the observations, and vary slightly (∼10%) depending on the way the UVS data is binned (e.g., longitudinal and emission angle binning).

The position of the MAW spot of the moons, together with a magnetic field model, is a key ingredient to estimate the equatorial lead angle, which is the focus of the next section.

4. Lead Angles

The equatorial lead angle (δ) is the angular separation between the position of the moon and the magnetically-mapped MAW footprint onto the orbital plane. The lead angle is determined by the sum of the physical processes occurring between the interaction region around the moon and Jupiter's ionosphere. In this work that uses Juno-UVS data, it is calculated by.

1. measuring the position of the MAW spot at a given time t_0,
2. determining the position of the moons at the same time t_0 from the ephemerides,
3. tracing back the position of the MAW spot in the moon orbital plane using a magnetic field model,
4. calculating the longitudinal difference between the moon and the back-traced MAW spot, hence the equatorial lead angle.

Juno in-situ instruments provided invaluable measurements of the particle distribution on the magnetic field lines connected to the satellite footprints and tails, such as measurements connected to Io (Clark et al., 2020; Szalay et al., 2018; Sulaiman et al., 2020, 2023; Szalay, Allegrini, et al., 2020b), Europa (Allegrini et al., 2020), and Ganymede (Hue et al., 2022; Louis et al., 2020; Szalay, Allegrini, et al., 2020a). Szalay, Allegrini, et al. (2020b) showed that the exponential decrease in precipitating electron energy flux, obtained from the Juno-JADE instrument when Juno was magnetically connected at various distances downstream the Io footprint tail, was better organized when considering the angular separation along Io's orbit between Io and an Alfvén wave back-traced from Jupiter's ionosphere to the moon orbital plane, as the power decays farther from the moons for each subsequent bounce of the initial Alfvén wave generated near the moon. Further, Sulaiman et al. (2023) showed the Poynting fluxes and field-aligned currents to similarly exhibit a decay as a function of the same downtail angle. That quantity, coined "Io-Alfvén tail distance" by Szalay, Allegrini, et al. (2020b), wraps up the knowledge of the equatorial lead angle within. Here, we provide critical updates unique to Juno's observational platform allowing for the calculation of Alfvén angles for Io, Europa, and Ganymede.

Figures 4 and 5 display the equatorial lead angle in the north and south, respectively, inferred from Juno-UVS and using the JRM33 magnetic field model (Connerney et al., 2022) combined with the Juno-era current sheet model (Connerney et al., 2020), and color-coded according to the perijove it was recorded at. The lead angle depends mainly on the travel time variation of the Alfvén waves through the higher plasma density region of the

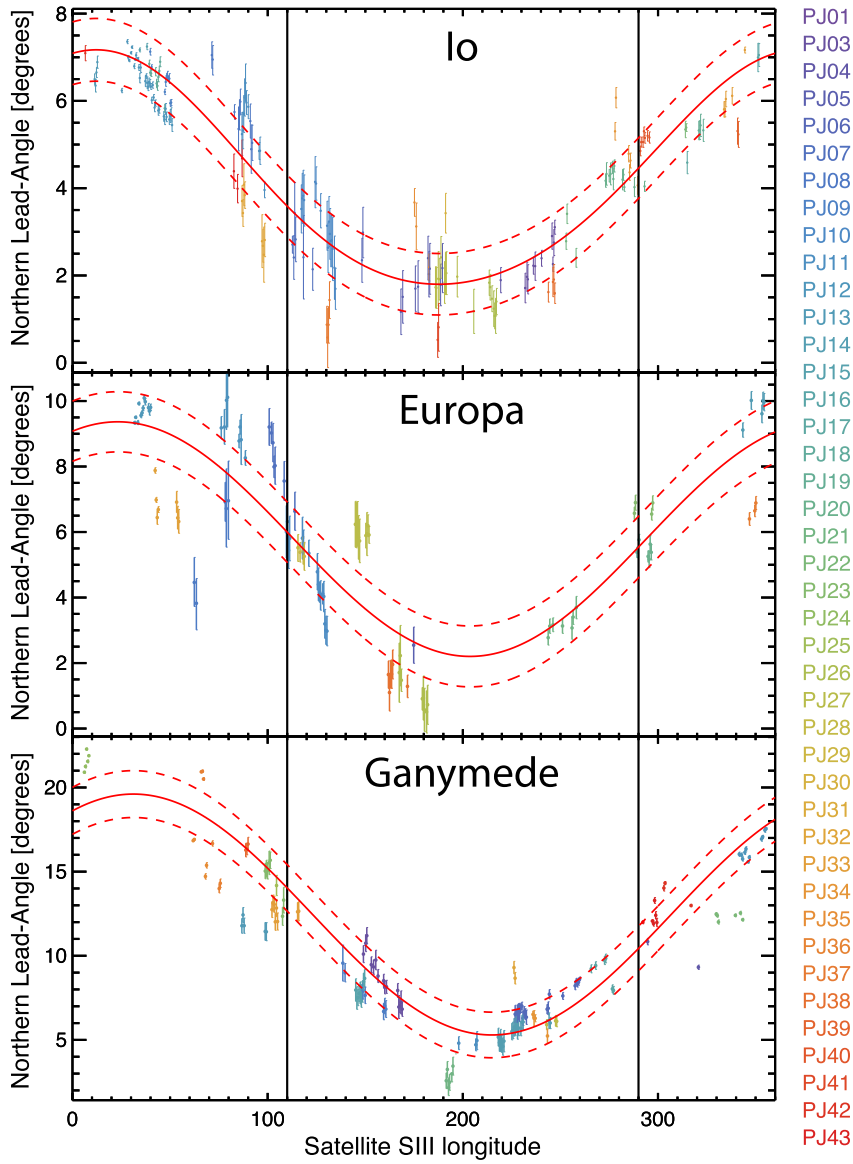

Figure 4. Northern lead angle for Io (top), Europa (middle), and Ganymede (bottom) using Juno-UVS dataset of the Main Alfvén Wing from PJ1 until PJ43. The vertical solid black lines indicate the location when the moons are at the center of the plasma sheet. The red lines correspond to the best fit obtained with Equation (3). The red-dashed lines correspond to the 3σ uncertainty on the fit parameters.

plasma sheet. Assuming a plasma sheet around Jupiter with uniform and constant plasma density to first order, one would expect a sinusoidal modulation of that angle with the latitudinal separation between the moons and the central part of the plasma sheet over the course of a Jovian rotation (Hess, Pétin, et al., 2010). Figures 4 and 5 are adjusted with a Fourier series, such that:

$$\delta = a_0 + \sum_{n=1}^{\infty} a_n \cos nw\lambda + b_n \sin nw\lambda \tag{3}$$

The best fit parameters of Equation 3 were estimates using a least-squares minimization technique (MPFIT package, Markwardt, 2009), and are listed on Table 1. In order to assume periodicity in the fit, the measured lead angles were replicated in the $[-2\pi: 4\pi]$ interval. Because of the sparsity of the Europa and Ganymede data, fitting the data with higher order Fourier series introduces oscillations. The lead angle data on these two moons is therefore fitted using a first order Fourier series. For Io, a second order Fourier series best reproduces the observations,

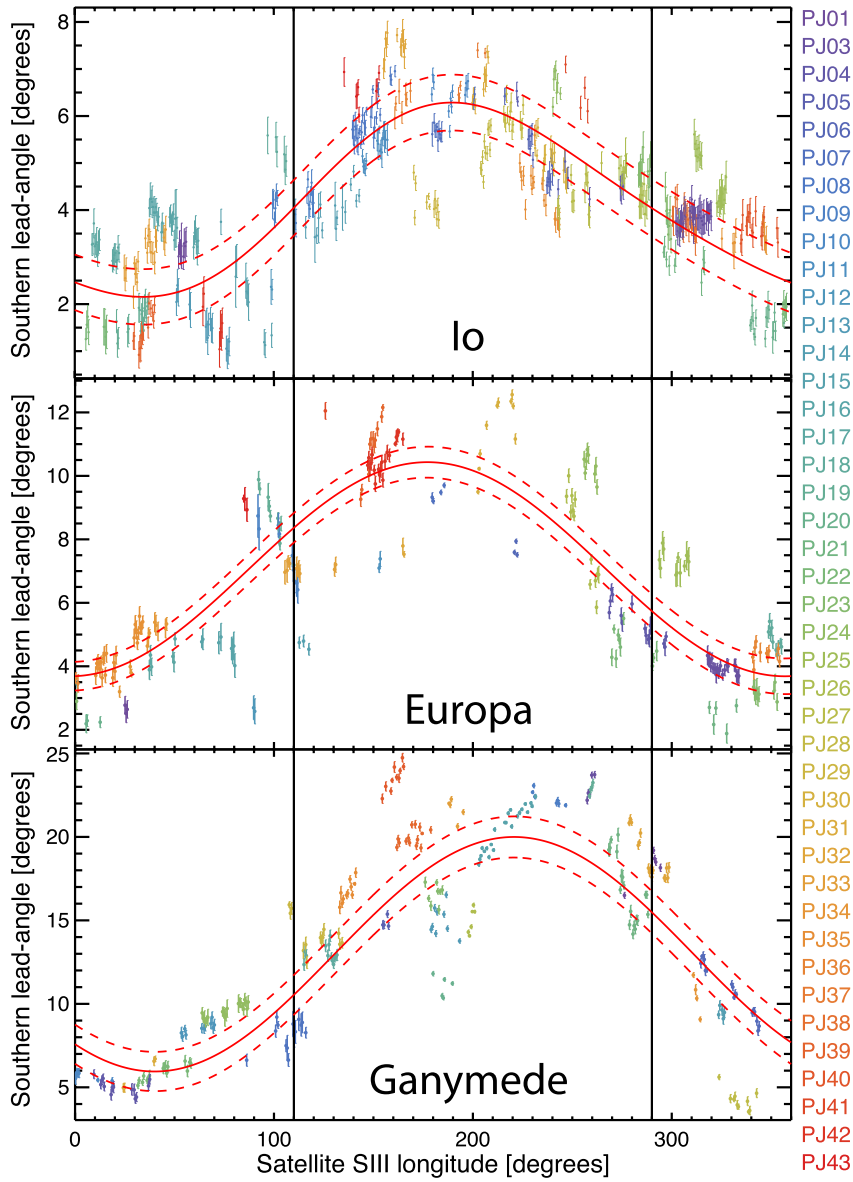

Figure 5. Same as Figure 4 for the south.

Table 1
Best Fit of the Northern and Southern Lead Angles for Io, Europa, and Ganymede, With λ the SIII West-Longitude of the Moon

	North	South
Io	$\delta = 4.26 + 2.64 \cos \lambda + 0.50 \sin \lambda + 0.20 \cos 2\lambda + 0.126 \sin 2\lambda$	$\delta = 4.14 - 1.89 \cos \lambda - 0.70 \sin \lambda + 0.22 \cos 2\lambda - 0.12 \sin 2\lambda$
Europa	$\delta = 5.78 + 3.29 \cos 0.99 \lambda + 1.41 \sin 0.99 \lambda$	$\delta = 7.06 - 3.37 \cos \lambda + 0.15 \sin \lambda$
Ganymede	$\delta = 12.45 + 6.16 \cos 0.98 \lambda + 3.64 \sin 0.98 \lambda$	$\delta = 12.97 - 5.39 \cos 0.99 \lambda - 4.50 \sin 0.99 \lambda$

based on the weighted sum of squared residuals, though producing larger uncertainties of the retrieved fit parameters.

The averaged values of the northern and southern Io lead angles are 4.3 ± 0.7° and 4.1 ± 0.6°, respectively. For Europa, these values are 5.8 ± 0.9° in the north, and 7.0 ± 0.5° in the south. For Ganymede, the averaged northern and southern lead angles are 12.3 ± 1.3° and 13.0 ± 1.3°, respectively. The uncertainties in the averaged lead angle is calculated using the 3-sigma uncertainties of the derived fit parameters, and are tighter in the south, due to the denser dataset. The averaged northern and southern lead angles value overlap for each individual moon, meaning that the Alfvén travel time is similar between hemispheres.

The Alfvén travel times can be approximated using measurements of the equatorial lead angle. The quantity $\delta_{moon}/360$ is the orbital fraction over

Table 2
Range of Northern and Southern Hemisphere Alfvén Travel Times for Io, Europa, and Ganymede Estimated From the Measured Lead Angles

	North	South
Io	$t_A^{min} = 3.9 \pm 1.5$ min	$t_A^{min} = 4.6 \pm 1.3$ min
	$t_A^{max} = 15.4 \pm 1.5$ min	$t_A^{max} = 13.5 \pm 1.3$ min
Europa	$t_A^{min} = 4.1 \pm 1.7$ min	$t_A^{min} = 6.9 \pm 1.0$ min
	$t_A^{max} = 17.5 \pm 1.7$ min	$t_A^{max} = 19.5 \pm 0.9$ min
Ganymede	$t_A^{min} = 9.3 \pm 2.4$ min	$t_A^{min} = 10.4 \pm 2.0$ min
	$t_A^{max} = 34.4 \pm 2.4$ min	$t_A^{max} = 35.1 \pm 2.2$ min

which the Alfvén wave travels from the interaction region to the Jovian ionosphere. If the moons were static, or far slower than the angular rotation of Jupiter, the Alfvén travel times could be estimated by multiplying this ratio by the Jovian orbital period. However, since the orbital period of the moon is not negligible when compared with the Jovian rotation period (especially for Io), the synodic period of the moon has to be accounted for. The Alfvén travel times can then be approximated using Equation (4).

$$t_A = \frac{P_{moon}^{syn} \times \delta_{moon}}{360}, \quad (4)$$

where P_{moon}^{syn} is the synodic period and δ_{moon} the measured equatorial lead angle of the moon of interest. The range of Alfvén travel times are listed in Table 2, and displayed in Figure 6. The derived Io Alfvén travel times are consistent with the modeled travel times by Hinton et al. (2019).

The lead angle shows considerable variability at a given SIII longitude, well beyond the observational uncertainties. Since this quantity accounts for the sum of the physical processes occurring between the interaction region around the moon and Jupiter's ionosphere, it is affected by plasma density variations encountered by the Alfvén waves within the torus and potential magnetic field strength variations. For Io, Hinton et al. (2019) estimated that the Alfvén travel times to Jupiter's southern ionosphere at $\lambda_{Io} = 200°$ ranged from 11 to 13.5 min solely based on torus density variations on the order of 50% caused by variation in Io's volcanic activity (Yoshikawa et al., 2017). Based on Io's synodic period, a 2.5 min variation in Alfvén travel times corresponds to a longitudinal shift of about 1.5°, which is fully consistent with the lead angle variations observed between perijoves. However, Hinton et al. (2019) also predicted a variation in the Alfvén travel times to Jupiter's southern ionosphere at $\lambda^{Io} = 30°$ from 2 to 3 min, leading to a predicted shift in lead angle of 0.6°, which appears smaller than the measured variation in lead angle in that longitude sector. The origin of this discrepancy is not clear, and could be due to either underestimating the uncertainties of the lead angle, uncertainties in the magnetic field model or simplifications in modeling the plasma sheet spatial variability.

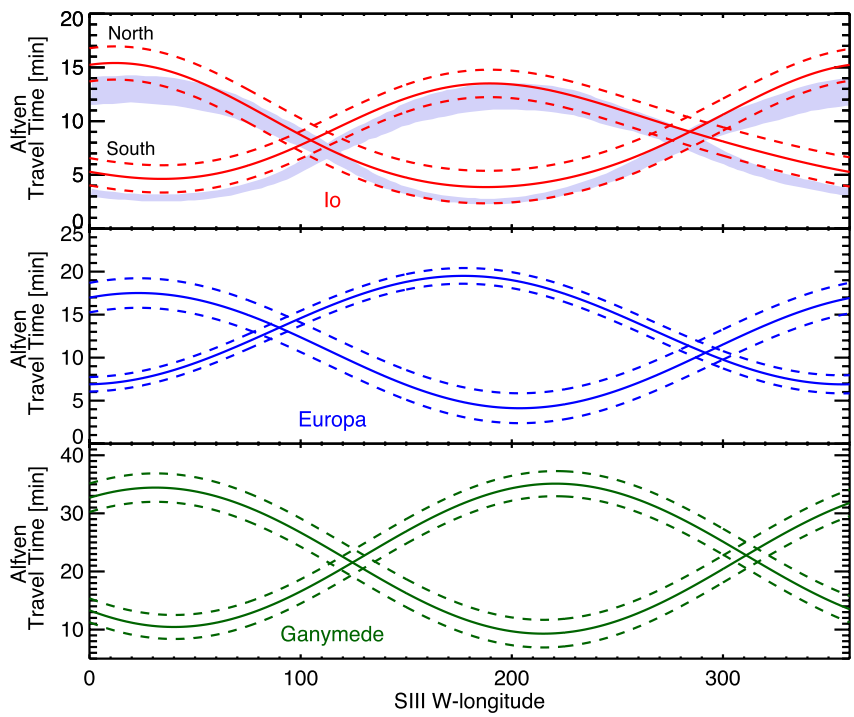

Figure 6. Alfvén travel times for Io (top), Europa (middle), and Ganymede (bottom), estimated from the equatorial lead angles measured by UVS. Blue-shaded area for Io comes from Hinton et al. (2019).

5. Variability in Magnetospheric Conditions and Lead Angle

The scatter in lead angle shown in Figures 4 and 5 implies significant variations in the magnetospheric conditions at the moons. Because the lead angle depends on the Alfvén travel times from the interaction region to the ionosphere, any temporal or spatial changes in the plasma density, structure of the plasma sheet, or even magnitude of the magnetic field in these regions need to be considered. We briefly discuss here the spatial and/or temporal variations of such quantities.

Neutrals escaping Io are dissociated and ionized by impacts from magnetospheric electrons (Bagenal & Dols, 2020). They are then picked up by the rotating magnetic field and brought up to near-corotation by transferring angular momentum from the Jovian ionosphere to the magnetosphere through a system of field-aligned currents, and regulated by the ionospheric conductivity (Hill, 1979). The radial transport of plasma then occurs through the centrifugally-driven flux tube interchange, in which plasma-loaded flux tube moves radially outward from its production source by the $\mathbf{E} \times \mathbf{B}$ drift, and are replaced by inward-moving flux tubes containing less mass (e.g., Thomas et al., 2004). The typical transport timescale of plasma from the Io to the Europa orbital distances was estimated to be in the ∼30–80 days (Bagenal & Delamere, 2011).

Plasma survey at various distances across the magnetosphere have been performed thanks to the previous Jupiter missions, and is being extended now with Juno (see, e.g., reviews of Bagenal et al., 2015; Bagenal & Dols, 2020). Density in the plasma sheet generally decreases by five orders of magnitude from $6\,R_J$ to $30\,R_J$ (Bagenal et al., 2016). Because of Jupiter's magnetic dipole tilt, magnetic field measurements from in-situ spacecrafts are characterized by regular sign changes in the radial component of that field associated with a plasma sheet crossing. Although previous in-situ plasma measurements performed in the middle magnetosphere of Jupiter showed a well-structured plasma sheet, variations in magnetic field measurements have been reported, indicating spatial and temporal variations of the current sheet position (e.g., Krupp et al., 2004).

Since the early Pioneer 10 and 11 missions, the magnetic field has been known to be distorted near the centrifugal equator, where the field is radially stretched outwards by the presence of the plasma sheet currents. An empirical model of the magnetodisk using the Voyagers measurements that accounts for a system of azimuthal currents circulating in the centrifugal equator were constructed to account for this effect (Connerney et al., 1981). The extensive data collected by Juno demonstrates that the magnetic field in the middle magnetosphere is less stretched than previously thought. This led Connerney et al. (2020) to revise the empirical magnetodisk model, and to add a radial current that contributes to the azimuthal component of the magnetic field (B_Φ), and designed to account for the transfer of angular momentum of the radially outflowing plasma. Orbit-by-orbit measurements of the radial current system contributing to the B_Φ component show significant variations, which might suggest a modulation in the angular momentum transfer that affects the plasma outflow (Connerney et al., 2020). Vogt et al. (2022) used magnetic field measurements from Juno as well as previous missions to survey the magnetic field condition near the orbit of Ganymede. They found that the expected temporal variability obtained from fit of the current sheet results in a 10–20% variability in the magnetic field components, and is longitude-dependent. Understanding and tracking the variability of the plasma sheet current is crucial as they may induce a displacement of the footprint location, especially for Ganymede (Promfu et al., 2022; Vogt et al., 2022). The variation in the Ganymede footprint position are large enough to be easily detected and thus is important to track magnetospheric changes.

Huscher et al. (2021) used Juno-JADE data at or near the plasma sheet crossing to survey the plasma density from Juno's first 26 orbits at radial distances beyond $17\,R_J$. The plasma sheet density structure can show significant variability in spatial structure, sometimes smaller than $1\,R_J$, over timescale of minutes, and between Juno orbits. At the same radial distance within the plasma sheet, the peak charged density of heavy ions measured by Juno-JADE can differ by about one order of magnitude between orbits. For instance, data from a few number of orbits indicated plasma density uniformly low (e.g., PJ12 and PJ26). Juno will be traversing the equatorial Io-Europa region as the extended mission progresses, and more results are expected.

In order to investigate temporal variability in the plasma sheet properties, Figure 7 present the lead angle deviations from the best fit obtained on Figures 4 and 5. Juno-UVS lead angle measurement is subtracted from the lead angle fit at the particular λ the data was recorded at. A positive/negative value for that quantity, called here Δ_{LA}, corresponds to the case where the Alfvén travel time was longer/shorter than the travel time derived from Equation (4), respectively. A longer Alfvén travel time may translate into the situation where either (a) the local plasma

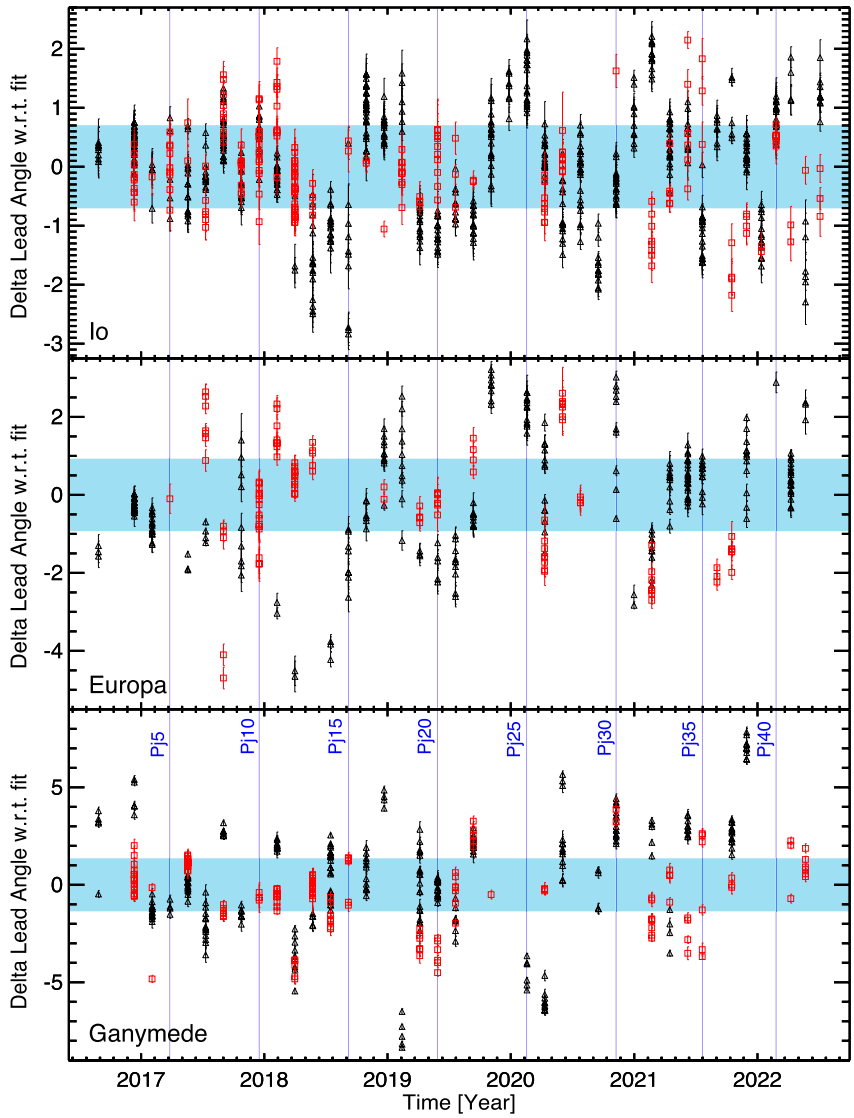

Figure 7. Time series of the measured lead angle deviation from the best fit shown in Figures 4 and 5. Red squares and black triangles correspond to the northern and southern lead angle data. The blue-shaded regions correspond to the uncertainty from the northern lead angle fit parameters shown in Figure 4.

sheet density was higher than nominal, (b) the plasma sheet vertical extent increased, (c) the local magnetic field amplitude decrease with respect to it nominal value, or a combination thereof.

The consistently lower density reported by Huscher et al. (2021) using Juno-JADE during the inbound section of Juno's orbit 12 throughout the magnetosphere may cause the Alfvén travel time to become temporarily shorter for that orbit, until the plasma density return to their nominal level. This would translate to a negative Δ_{LA}, and is roughly consistent with the Δ_{LA} measured for Io (south), Europa (south), and Ganymede (both north and south) on PJ12. A couple of issues with that interpretation are that (a) Juno-JADE only measured the densities from 17 to 50 R_J, that is, from Ganymede and beyond, (b) the JADE data were recorded several days prior to the UVS data (1–3 days, depending on the orbit number). Lower plasma density in the middle magnetosphere measured by JADE may be a consequence of a temporary slowdown of the mass loading from Io, implying lower densities in the inner magnetosphere prior to PJ12. This means that UVS should have recorded consistently negative Δ_{LA} on, for example, PJ11, which is not the case.

Although no clear temporal trends can be distinguished from Figure 7, a Lomb–Scargle periodogram analysis on these time-series reveals a period in the 400–500 days range for Io. This may be consistent with the periodic

brightening of Loki Patera, the most powerful volcano on Io, as monitored in the infrared. The periodicity of such brightness was thought to be correlated with periodic changes in Io's eccentricity and semimajor axis, about 480 and 460 days, respectively (de Kleer et al., 2019). Io is the main supplier of plasma in the Jovian magnetosphere. Changes in Io's volcanic activity affect the radial circulation of mass and energy in the middle magnetosphere over time scales of tens of days. For instance, De Kleer and De Pater (2016) have characterized the location and appearance of hot spots on Io in the near-IR and found widespread activity from August–September 2013 and from October 2014 to May 2015. Around the same time, the Hisaki telescope monitored the torus ion emission lines of the Jovian system in the 55–145 nm range (Yoshikawa et al., 2014). Enhancements in the sodium emission line (Yoneda et al., 2015), as well as sulfur and oxygen emission lines (Tsuchiya et al., 2018) was detected from mid-Jan until mid-Mar 2015, over sensibly different timescales. During the Cassini era, temporal changes in the emissions from the major sulfur and oxygen ions torus species was suggested to be related to the changes in outgassing from Io (Delamere et al., 2004; Steffl et al., 2006). However, tying together changes in the brightness of Io's volcanoes with enhancements in the various emission lines of the torus (e.g., sodium, oxygen, and sulfur), to ultimately derive changes in mass supplied to the torus is not straightforward and still unclear.

The present work provides an empirical fit of the equatorial lead angle for Io, Europa, and Ganymede derived from Juno data, from which the averaged Alfvén travel time is derived. It also demonstrates how, by accounting for these lead angle values, the interpretation of the moon-induced decametric radio emissions can be improved, as demonstrated below. Understanding the effect of magnetospheric conditions on the lead angle variability is beyond the scope of this work, and deserves a dedicated study.

6. Application to Modeling of the Moon-Induced Decametric Emission

The knowledge of the lead angle is also important for the interpretation of the moon-induced decametric emissions (e.g., Hess, Pétin, et al., 2010; Louis et al., 2019; Lamy et al., 2022; Marques et al., 2017). This section illustrates the added benefit from the equatorial lead angle knowledge in a case related to the interpretion of the Ganymede-induced decametric radio emission. These emissions are thought to originate from the cyclotron maser instability (CMI), a wave-particle instability where a circularly polarized wave resonates with the gyrating motion of an accelerated electron population (Treumann, 2006; Wu, 1985; Wu & Lee, 1979). That mechanism was confirmed using Juno in-situ measurements (Louarn et al., 2017; Louarn et al., 2018; Louis et al., 2020). These radio emissions are produced along the magnetic field lines, at a frequency close to the electron cyclotron frequency (proportional to the magnetic field amplitude), and beamed along the edges of a thin hollow cone on the order of a degree in thickness. The opening angle of this cone is dependent on the electron energy (Hess et al., 2008). In order to interpret the moon-induced decametric emission, modeling tools such as the Exoplanetary and Planetary Radio Emission Simulator (ExPRES, Hess et al., 2008; Louis et al., 2019) require knowledge of both the lead angle and electrons velocity. Because the directionality of these radio emissions depend both on the electron energy and the lead angle, this may lead to situations where non-unique solutions exist, in order to reproduce the observed decametric radio arcs. The knowledge of the active field line (where the radio emission sources are located) and thus the lead angle, constitutes one of the main sources of uncertainty in determining the electron energy responsible for the radio emission (Hess, Pétin, et al., 2010; Lamy et al., 2022). Previous estimate of the absolute lead angle values were not accurate enough mostly because of the uncertainty in the magnetic field models as well as the uncertainties in the Europa and Ganymede measured footprint positions from HST (Hess, Pétin, et al., 2010), leading to non-physical cases with negative lead-angle.

Several datasets of moon-induced decametric radio emission were recorded by the Radio and Plasma Wave Science (RPWS) instrument on Cassini (Gurnett et al., 2004) on 17 November 2000, prior to the Jupiter flyby. Figure 8 shows the analysis of a decametric arc induced by Ganymede, and previously studied by Louis et al. (2017). RPWS data is shown on panels A and B as time-frequency spectrograms, corresponding to a Ganymede-D decametric arc, that is, emitted on a field line connecting Ganymede and Jupiter's southern hemisphere around Jupiter's dawn side. Because the waves amplified by the cyclotron maser instability are circularly polarized, panel A shows the time-frequency spectrogram corresponding to the degree of circular polarization, for better contrast. During the observation of the Ganymede-D arc (from ∼22:00 to ∼02:00), the longitude of Ganymede varies from 348° to 133°.

Panel C shows the best fit to the data, prior to this work, using the ExPRES radio modeling (Louis et al., 2019). This assumes (a) the radio emission is created by a loss-cone electron distribution with energies of 3 keV, (b)

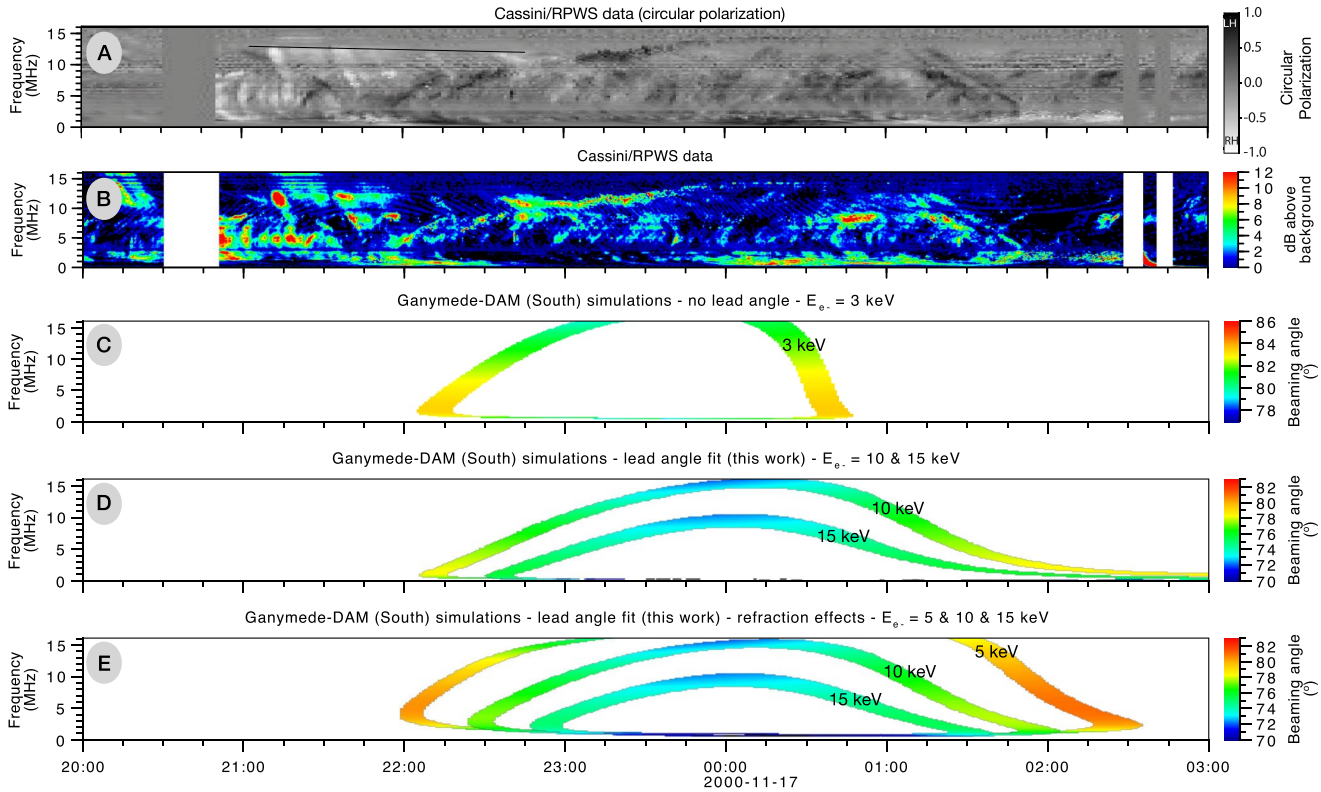

Figure 8. Panel (a) Cassini-RPWS time-frequency spectrogram of circularly polarized radio emission. Panel (b) Cassini-RPWS time-frequency spectrogram. Panel (c) ExPRES simulation of a Ganymede-D decametric arc without lead angle. Panel (d) ExPRES simulation using the lead angle derived from this present study. Panel (e) ExPRES simulation combining the lead angle derived from this present and refraction effect on the emission. This simulations have been produced using the Version 1.2.0 of ExPRES (Louis et al., 2023).

the JRM33 magnetic field model, and (c) no equatorial lead angle. Note that we consider here a simplistic mono-energetic case, as Juno clearly observed electrons distributed as a power-law extending well above and below 3 keV (e.g., Szalay et al., 2018). Although it was previously presented by Louis et al. (2017), this application differs slightly from that earlier work which assumed the ISaAC magnetic field model (Hess et al., 2017). Panel (d) shows simulations using ExPRES considering the equatorial lead angle fit derived from the present work. The best fit of the data is obtained considering electrons with energies ranging from 10 to 15 keV. When accounting for refraction effects on the beamed radio emissions, the fit can be improved by considering electrons of energies ranging 5–15 keV (panel e). Refraction effects are occurring when the radio emissions are emitted in a region with decreasing electron cyclotron frequency (f_{ce}). In which case, the emission cannot propagate due to the cut-off frequency at f_{ce}, and the radio wave is reflected until it reaches a region with increasing f_{ce} (Galopeau & Boudjada, 2016; Louis, Lamy, Zarka, Cecconi, Imai, et al., 2017; Louis et al., 2021).

The addition of the knowledge on the equatorial angle, especially for Europa and Ganymede, improves the predictability and analysis of moon-induced decametric radio emission. Due to Ganymede's longitude variation during the observation of the Ganymede-D arc, based on our new lead angle model, the error on the active magnetic field line position goes from 5° (minimal value of δ in the south) to 14°, which lead to a poor estimate on the location of the sources. Since the shape of the arc depends mainly on the lead angle (position of the active field line), the magnetic field model (value of B, and therefore position of the sources, along the field line) and the energy of the electrons (value of the emission cone aperture), a too low estimate of the longitude of the active field line will lead to an underestimation of the value of the energy of the electrons (Hess, Pétin, et al., 2010; Louis et al., 2017). This is what is noted in the simulations comparing Figures 8a and 8c, where a lower value of electrons is needed to fit correctly the arc without a lead angle model.

This improved estimation of the position of the active field lines, and therefore of the position of the radio sources, allows reducing the number of unknowns and to obtain a better, and more reliable, estimate of the electron energy.

For instance, comparing in more details the simulations that account for the lead angle and refractions effects (Figure 8c) with the circularly polarized radio emission from RPWS indicates that the early part of the radio emission arc (from 22:00:00 to 22:15:00) are better reproduced with electrons with lower energies, that is, 5 keV, while the center and end of the arc are better reproduced with electrons with energies ranging from 10 to 15 keV. It is worth noting here that Lamy et al. (2022) showed that, in the case of Io, the electrons energy derived from radio emission analysis is variable as a function of the moon longitude. It is not surprising here to observe that in order to reproduce the arc in the time-frequency plane, the energy of the electrons must vary with time (*i.e.,* the longitude of the moon). Finally, the ExPRES simulations with the new lead angle model give results that are in agreement with the Juno in-situ observations recorded during a Ganymede fluxtube crossing on PJ20, on 29 May 2019 (Louis et al., 2020).

7. Discussion and Summary

The presented work makes use of 479 and 1148 individual spectral images of the satellite footprints recorded over the northern and southern auroral regions, respectively, measured by Juno-UVS from PJ1 to PJ43 (at the exception of PJ2), that is, about 6 years of Juno data. From these images, the accurate positions of the Io, Europa and Ganymede MAW spots are estimated and compared with the prediction from the magnetic field model obtained at the end of Juno's prime mission, JRM33 (Connerney et al., 2022). The accuracy with predictions from JRM33 can be estimated while limiting the projection effect by restricting to data recorded at small emission angles. We selected data points with emission angle lower than 20°, which allowed us to reduce the uncertainty associated to the projected vertical extent of the footprint emission curtain (σ_P in 2) while keeping enough data to perform a statistical analysis. In general, the average distance between the JRM33-computed moon footpaths and the observed MAW positions is smaller than 500 km, which is equivalent to <0.4° on Jupiter.

Measurements of the equatorial lead angle provide information on how the Alfvén waves generated around the moon interaction region propagate toward the Jovian ionosphere. It is an important piece of information for (a) interpreting the footprint related in-situ measurements made by Juno, (b) inferring in-situ conditions of the plasma sheet (e.g., a lead angle greater than the fit derived here might be caused by a higher than usual plasma density, or a variation in the magnetic field strength), and (c) analyzing the satellite-induced decametric radio emission. Despite the variability in the measured lead angle at a given moon longitude, a statistically consistent trend can be derived from the first 43 perijoves. The best fit of the lead angle for Io is in the 1.8°–7.2° range, with an average calculated as the arithmetic mean of 4.2°. For Europa, the lead angle ranges from 2.2° to 10.4°, with an average of 6.4°. For Ganymede, the lead angle is in the 5.3°–20.0° range, with an average of 12.7°. Over an entire Jovian rotation, this corresponds to Alfvén travel times ranging from 3.9 to 15.4 min, 4.1–19.5 min, and 9.3–35.1 min for Io, Europa, and Ganymede, respectively.

Significant deviations of the lead angle at a given longitude were observed for all moons. Changes in the magnetospheric conditions, such as plasma density variations, magnetic field amplitude or spatial structure of the plasma sheet, are likely responsible for such variations. Comparing the instantaneous lead angle obtained from the observed MAW footprint positions with the fit derived may provide an indication of these changes in magnetospheric conditions. Time series of the lead angle variation with respect to the best fit does not show a consistent temporal trend for Europa and Ganymede (see Figure 7). For Io, a Fourier analysis shows a tentative periodic change in the 400–500 days range, which may be attributed to modulated in Io's volcanic activity, although a dedicated study on this topic is beyond the scope of this investigation and deserves a detailed examination.

Modeling the moon-induced decametric arc requires the knowledge of the equatorial lead angle to constrain with higher accuracy the derived electron energy causing the emission. When accounting for the equatorial lead angle values from this work in the ExPRES simulation tool, the derived electron energy required to reproduce the Ganymede-induced decametric arc is in agreement with the in-situ measured values from Juno. This method can be applied for modeling the moon-induced radio emission for which no in-situ particle measurements data is available.

The main conclusions of this work are listed as follows.

1. The reported position of the MAW spots for Io, Europa, and Ganymede agrees well with the JRM33-computed satellite footpath generally <500 km, which is equivalent to <0.4° on Jupiter.

2. Empirical formulae for the Io, Europa, and Ganymede equatorial lead angles derived from Juno data are provided.
3. The range of equatorial lead angle for Io, Europa, and Ganymede is 1.8°–7.2°, 2.2°–10.4°, 5.3°–20.0°, respectively.
4. The respective range of Alfvén travel times for Io, Europa, and Ganymede, derived from the lead angle, are 3.9–15.4 min, 4.1–19.5 min, and 9.3–35.1 min.
5. Knowledge of the lead angle allows, for example, better simulating the decametric radio emission induced by the Galilean moons. By comparing them with the observations, this makes possible deriving more precisely the energies of the electrons triggering these emissions. This new derivation is in agreement with the Juno in-situ measurements.

Data Availability Statement

All the data used in this study are publicly available on the PDS Atmospheres Node Data Set Catalog https://pds-atmospheres.nmsu.edu/cgi-bin/getdir.pl?dir=DATA&volume=jnouvs_3001. Juno-UVS calibrated data (Reduced Data Record) recorded during Juno's perijove observation sequences were used here. The corresponding dataset used here contain the string *PXXOBS*, where XX = 1 to 43. Cassini/RPWS data display in this article are part of the Cecconi et al. (2017) collection, and has been produced following the "Circular Polarization mode" goniopolarimetric Inversion described in Section 2.1.3.2 of Cecconi and Zarka (2005).

Acknowledgments
We are grateful to NASA and contributing institutions that have made the Juno mission possible. This work was funded by the NASA's New Frontiers Program for Juno via contract NNM06AA75C with the Southwest Research Institute. CKL's work at the Dublin Institute for Advanced Studies was funded by Science Foundation Ireland Grant 18/FRL/6199. AHS acknowledges NASA NFDAP Grant 80NSSC23K0276. Hue acknowledges support from the French government under the France 2030 investment plan, as part of the Initiative d'Excellence d'Aix-Marseille Université – A*MIDEX AMX-22-CPJ-04.

References

Acton, C., Bachman, N., Semenov, B., & Wright, E. (2018). A look towards the future in the handling of space science mission geometry. *Planetary and Space Science*, *150*, 9–12. https://doi.org/10.1016/j.pss.2017.02.013

Acton, C. H. (1996). Ancillary data services of NASA's navigation and ancillary information facility. *Planetary and Space Science*, *44*(1), 65–70. https://doi.org/10.1016/0032-0633(95)00107-7

Acuna, M. H., Behannon, K. W., & Connerney, J. E. P. (1983). Physics of the Jovian magnetosphere. 1. Jupiter's magnetic field and magnetosphere. In *Physics of the jovian magnetosphere* (pp. 1–50).

Acuna, M. H., Neubauer, F. M., & Ness, N. F. (1981). Standing Alfvén wave current system at Io. *Voyager 1 Observations*, *86*(A10), 8513–8521. https://doi.org/10.1029/JA086iA10p08513

Allegrini, F., Gladstone, G. R., Hue, V., Clark, G., Szalay, J. R., Kurth, W. S., et al. (2020). First report of electron measurements during a Europa footprint tail crossing by Juno. *Geophysical Research Letters*, *47*(18), e89732. https://doi.org/10.1029/2020GL089732

Bagenal, F., Adriani, A., Allegrini, F., Bolton, S. J., Bonfond, B., Bunce, E. J., et al. (2017). Magnetospheric science objectives of the Juno mission. *Space Science Reviews*, *213*(1–4), 219–287. https://doi.org/10.1007/s11214-014-0036-8

Bagenal, F., & Delamere, P. A. (2011). Flow of mass and energy in the magnetospheres of Jupiter and Saturn. *Journal of Geophysical Research (Space Physics)*, *116*(A5), A05209. https://doi.org/10.1029/2010JA016294

Bagenal, F., & Dols, V. (2020). The space environment of Io and Europa. *Journal of Geophysical Research (Space Physics)*, *125*(5), e27485. https://doi.org/10.1029/2019JA027485

Bagenal, F., Sidrow, E., Wilson, R. J., Cassidy, T. A., Dols, V., Crary, F. J., et al. (2015). Plasma conditions at Europa's orbit. *Icarus*, *261*, 1–13. https://doi.org/10.1016/j.icarus.2015.07.036

Bagenal, F., Wilson, R. J., Siler, S., Paterson, W. R., & Kurth, W. S. (2016). Survey of Galileo plasma observations in Jupiter's plasma sheet. *Journal of Geophysical Research (Planets)*, *121*(5), 871–894. https://doi.org/10.1002/2016JE005009

Belcher, J. W. (1983). Physics of the Jovian magnetosphere. 3. The low-energy plasma in the Jovian magnetosphere. In *Physics of the Jovian magnetosphere* (pp. 68–105). https://doi.org/10.1017/cbo9780511564574.005

Belcher, J. W., Goertz, C. K., Sullivan, J. D., & Acuna, M. H. (1981). Plasma observations of the Alfvén wave generated by Io. *Journal of Geophysical Research*, *86*(A10), 8508–8512. https://doi.org/10.1029/JA086iA10p08508

Bigg, E. K. (1964). Influence of the satellite io on jupiter's decametric emission. *Nature*, *203*(4949), 1008–1010. https://doi.org/10.1038/2031008a0

Bolton, S. J., Adriani, A., Adumitroaie, V., Allison, M., Anderson, J., Atreya, S., et al. (2017). Jupiter's interior and deep atmosphere: The initial pole-to-pole passes with the Juno spacecraft. *Science*, *356*(6340), 821–825. https://doi.org/10.1126/science.aal2108

Bonfond, B. (2010). The 3-D extent of the Io UV footprint on Jupiter. *Journal of Geophysical Research (Space Physics)*, *115*(A9), A09217. https://doi.org/10.1029/2010JA015475

Bonfond, B., Gladstone, G. R., Grodent, D., Gérard, J. C., Greathouse, T. K., Hue, V., et al. (2018). Bar code events in the Juno-UVS data: Signature 10 MeV electron microbursts at Jupiter. *Geophysical Research Letters*, *45*(22), 12108–12115. https://doi.org/10.1029/2018GL080490

Bonfond, B., Gladstone, G. R., Grodent, D., Greathouse, T. K., Versteeg, M. H., Hue, V., et al. (2017). Morphology of the UV aurorae Jupiter during. *Juno's First Perijove Observations*, *44*(10), 4463–4471. https://doi.org/10.1002/2017GL073114

Bonfond, B., Grodent, D., Gérard, J. C., Radioti, A., Dols, V., Delamere, P. A., & Clarke, J. T. (2009). The Io UV footprint: Location, inter-spot distances and tail vertical extent. *Journal of Geophysical Research (Space Physics)*, *114*(A7), A07224. https://doi.org/10.1029/2009JA014312

Bonfond, B., Grodent, D., Gérard, J.-C., Radioti, A., Saur, J., & Jacobsen, S. (2008). UV Io footprint leading spot: A key feature for understanding the UV Io footprint multiplicity? *Geophysical Research Letters*, *35*(5), L05107. https://doi.org/10.1029/2007GL032418

Bonfond, B., Grodent, D., Gérard, J. C., Stallard, T., Clarke, J. T., Yoneda, M., et al. (2012). Auroral evidence of Io's control over the magnetosphere of Jupiter. *Geophysical Research Letters*, *39*(1), L01105. https://doi.org/10.1029/2011GL050253

Bonfond, B., Saur, J., Grodent, D., Badman, S. V., Bisikalo, D., Shematovich, V., et al. (2017). The tails of the satellite auroral footprints at Jupiter. *Journal of Geophysical Research (Space Physics)*, *122*(8), 7985–7996. https://doi.org/10.1002/2017JA024370

Bonfond, B., Yao, Z. H., Gladstone, G. R., Grodent, D., Gérard, J. C., Matar, J., et al. (2021). Are dawn storms Jupiter's auroral substorms? *AGU Advances*, *2*(1), e00275. https://doi.org/10.1029/2020AV000275

Cecconi, B., & Zarka, P. (2005). Direction finding and antenna calibration through analytical inversion of radio measurements performed using a system of 2 or 3 electric dipole antennas. *Radio Science - RADIO SCI*, *40*. https://doi.org/10.1029/2004RS003070
Cecconi, B., Zarka, P., Lamy, L., & Schippers, P. (2017). Cassini/rpws/hfr lesia/kronos collection (version 1.0) [dataset]. PADC, *40*. https://doi.org/10.25935/1SXH-AQ56
Clark, G., Mauk, B. H., Kollmann, P., Szalay, J. R., Sulaiman, A. H., Gershman, D. J., et al. (2020). Energetic proton acceleration associated with Io's footprint tail. *Geophysical Research Letters*, *47*(24), e90839. https://doi.org/10.1029/2020GL090839
Clarke, J. T., Ajello, J., Ballester, G., Ben Jaffel, L., Connerney, J., Gérard, J.-C., et al. (2002). Ultraviolet emissions from the magnetic footprints of Io. *Ganymede and Europa on Jupiter*, *415*(6875), 997–1000. https://doi.org/10.1038/415997a
Clarke, J. T., Ballester, G. E., Trauger, J., Evans, R., Connerney, J. E. P., Stapelfeldt, K., et al. (1996). Far-ultraviolet imaging of Jupiter's aurora and the lo "footprint". *Science*, *274*(5286), 404–409. https://doi.org/10.1126/science.274.5286.404
Connerney, J. E. P., Acuna, M. H., & Ness, N. F. (1981). Modeling the Jovian current sheet and inner magnetosphere. *Journal of Geophysical Research*, *86*(A10), 8370–8384. https://doi.org/10.1029/JA086iA10p08370
Connerney, J. E. P., Acuña, M. H., Ness, N. F., & Satoh, T. (1998). New models of Jupiter's magnetic field constrained by the Io flux tube footprint. *Journal of Geophysical Research*, *103*(A6), 11929–11939. https://doi.org/10.1029/97JA03726
Connerney, J. E. P., Adriani, A., Allegrini, F., Bagenal, F., Bolton, S. J., Bonfond, B., et al. (2017). Jupiter's magnetosphere and aurorae observed by the Juno spacecraft during its first polar orbits. *Science*, *356*(6340), 826–832. https://doi.org/10.1126/science.aam5928
Connerney, J. E. P., Baron, R., Satoh, T., & Owen, T. (1993). Images of excited H^{3+} at the foot of the Io flux tube in Jupiter's atmosphere. *Science*, *262*(5136), 1035–1038. https://doi.org/10.1126/science.262.5136.1035
Connerney, J. E. P., Timmins, S., Herceg, M., & Joergensen, J. L. (2020). A Jovian magnetodisc model for the Juno era. *Journal of Geophysical Research (Space Physics)*, *125*(10), e28138. https://doi.org/10.1029/2020JA028138
Connerney, J. E. P., Timmins, S., Oliversen, R. J., Espley, J. R., Joergensen, J. L., Kotsiaros, S., et al. (2022). A new model of Jupiter's magnetic field at the completion of Juno's prime mission. *Journal of Geophysical Research (Planets)*, *127*(2), e07055. https://doi.org/10.1029/2021JE007055
Crary, F. J., & Bagenal, F. (1997). Coupling the plasma interaction at io to jupiter. *Geophysical Research Letters*, *24*(17), 2135–2138. https://doi.org/10.1029/97GL02248
Damiano, P. A., Delamere, P. A., Stauffer, B., Ng, C. S., & Johnson, J. R. (2019). Kinetic simulations of electron acceleration by dispersive scale. *Alfvén Waves in Jupiter's Magnetosphere.*, *46*(6), 3043–3051. https://doi.org/10.1029/2018GL081219
Davis, M. W., Gladstone, G. R., Greathouse, T. K., Slater, D. C., Versteeg, M. H., Persson, K. B., et al. (2011). Radiometric performance results of the Juno ultraviolet spectrograph (Juno-UVS). *SPIE Proceedings*, *8146*, 814604. https://doi.org/10.1117/12.894274
De Kleer, K., & De Pater, I. (2016). Time variability of Io's volcanic activity from near-IR adaptive optics observations on 100 nights in 2013-2015. *Icarus*, *280*, 378–404. https://doi.org/10.1016/j.icarus.2016.06.019
De Kleer, K., Nimmo, F., & Kite, E. (2019). Variability in Io's volcanism on timescales of periodic orbital changes. *Geophysical Research Letters*, *46*(12), 6327–6332. https://doi.org/10.1029/2019GL082691
Delamere, P. A., Bagenal, F., Ergun, R., & Su, Y. J. (2003). Momentum transfer between the Io plasma wake and Jupiter's ionosphere. *Journal of Geophysical Research (Space Physics)*, *108*(A6), 1241. https://doi.org/10.1029/2002JA009530
Delamere, P. A., Steffl, A., & Bagenal, F. (2004). Modeling temporal variability of plasma conditions in the Io torus during the Cassini era. *Journal of Geophysical Research (Space Physics)*, *109*(A10), A10216. https://doi.org/10.1029/2003JA010354
Dessler, A. J. (1983). Coordinate systems. In A. J. Dessler (Ed.), *Physics of the jovian magnetosphere* (pp. 498–504). Cambridge University Press. https://doi.org/10.1017/CBO9780511564574.016
Ebert, R. W., Greathouse, T. K., Clark, G., Hue, V., Allegrini, F., Bagenal, F., et al. (2021). Simultaneous UV images and high-latitude particle and field measurements during an auroral dawn storm at Jupiter. *Journal of Geophysical Research (Space Physics)*, *126*(12), e29679. https://doi.org/10.1029/2021JA029679
Galopeau, P. H. M., & Boudjada, M. Y. (2016). An oblate beaming cone for Io-controlled Jovian decameter emission. *Journal of Geophysical Research (Space Physics)*, *121*(4), 3120–3138. https://doi.org/10.1002/2015JA021038
Gérard, J.-C., Saglam, A., Grodent, D., & Clarke, J. T. (2006). Morphology of the ultraviolet Io footprint emission and its control by Io's location. *Journal of Geophysical Research (Space Physics)*, *111*(A4), A04202. https://doi.org/10.1029/2005JA011327
Gershman, D. J., Connerney, J. E. P., Kotsiaros, S., DiBraccio, G. A., Martos, Y. M., Viñas, A. F., et al. (2019). Alfvénic fluctuations associated with Jupiter's. *Auroral Emissions*, *46*(13), 7157–7165. https://doi.org/10.1029/2019GL082951
Gladstone, G. R., Persyn, S. C., Eterno, J. S., Walther, B. C., Slater, D. C., Davis, M. W., et al. (2017). The ultraviolet spectrograph on NASA's Juno mission. *Space Science Reviews*, *213*(1–4), 447–473. https://doi.org/10.1007/s11214-014-0040-z
Goldreich, P., & Lynden-Bell, D. (1969). Io: A Jovian unipolar inductor. *The Astrophysical Journal*, *156*, 59. https://doi.org/10.1086/149947
Greathouse, T. K., Gladstone, G. R., Davis, M. W., Slater, D. C., Versteeg, M. H., Persson, K. B., et al. (2013). Performance results from in-flight commissioning of the Juno ultraviolet spectrograph (Juno-UVS). *UV, x-ray, and gamma-ray space instrumentation for astronomy xviii*, *8859*, 88590T. https://doi.org/10.1117/12.2024537
Grodent, D., Bonfond, B., GéRard, J.-C., Radioti, A., Gustin, J., Clarke, J. T., et al. (2008). Auroral evidence of a localized magnetic anomaly in Jupiter's northern hemisphere. *Journal of Geophysical Research (Space Physics)*, *113*(A9), A09201. https://doi.org/10.1029/2008JA013185
Gurnett, D. A., & Goertz, C. K. (1981). Multiple Alfven wave reflections excited by Io: Origin of the Jovian decametric arcs. *Journal of Geophysical Research*, *86*(A2), 717–722. https://doi.org/10.1029/JA086iA02p00717
Gurnett, D. A., Kurth, W. S., Kirchner, D. L., Hospodarsky, G. B., Averkamp, T. F., Zarka, P., et al. (2004). The Cassini radio and plasma wave investigation. *Space Science Reviews*, *114*(1–4), 395–463. https://doi.org/10.1007/s11214-004-1434-0
Hess, S., Cecconi, B., & Zarka, P. (2008). Modeling of Io-Jupiter decameter arcs. *emission beaming and energy source*, *35*(13), L13107. https://doi.org/10.1029/2008GL033656
Hess, S. L. G., Bonfond, B., Bagenal, F., & Lamy, L. (2017). A model of the Jovian internal field derived from in-situ and auroral constraints. In G. Fischer, G. Mann, M. Panchenko, & P. Zarka (Eds.), *Planetary radio emissions viii* (pp. 157–167). https://doi.org/10.1553/PRE8s157
Hess, S. L. G., Bonfond, B., Chantry, V., Gérard, J.-C., Grodent, D., Jacobsen, S., & Radioti, A. (2013). Evolution of the Io footprint brightness II: Modeling. *Planetary and Space Science*, *88*, 76–85. https://doi.org/10.1016/j.pss.2013.08.005
Hess, S. L. G., Bonfond, B., Zarka, P., & Grodent, D. (2011). Model of the Jovian magnetic field topology constrained by the Io auroral emissions. *Journal of Geophysical Research (Space Physics)*, *116*(A5), A05217. https://doi.org/10.1029/2010JA016262
Hess, S. L. G., Delamere, P., Dols, V., Bonfond, B., & Swift, D. (2010). Power transmission and particle acceleration along the Io flux tube. *Journal of Geophysical Research (Space Physics)*, *115*(A6), A06205. https://doi.org/10.1029/2009JA014928
Hess, S. L. G., Pétin, A., Zarka, P., Bonfond, B., & Cecconi, B. (2010). Lead angles and emitting electron energies of Io-controlled decameter radio arcs. *Planetary and Space Science*, *58*(10), 1188–1198. https://doi.org/10.1016/j.pss.2010.04.011
Hill, T. W. (1979). Inertial limit on corotation. *Journal of Geophysical Research*, *84*(A11), 6554–6558. https://doi.org/10.1029/JA084iA11p06554

Hill, T. W., & Vasylinas, V. M. (2002). Jovian auroral signature of Io's corotational wake. *Journal of Geophysical Research*, *107*(A12), SMP271–SMP275. https://doi.org/10.1029/2002JA009514

Hinton, P. C., Bagenal, F., & Bonfond, B. (2019). Alfvén wave propagation in the io plasma torus. *Geophysical Research Letters*, *46*(3), 1242–1249. https://doi.org/10.1029/2018GL081472

Hue, V., Giles, R. S., Gladstone, G. R., Greathouse, T. K., Davis, M. W., Kammer, J. A., & Versteeg, M. H. (2021). Updated radiometric and wavelength calibration of the Juno ultraviolet spectrograph. *Journal of Astronomical Telescopes, Instruments, and Systems*, *7*(04), 044003. https://doi.org/10.1117/1.JATIS.7.4.044003

Hue, V., Gladstone, G. R., Greathouse, T. K., Kammer, J. A., Davis, M. W., Bonfond, B., et al. (2019). Flight characterization and calibration of the Juno-ultraviolet spectrograph (Juno-UVS). *AJ*, *157*(2), 90. https://doi.org/10.3847/1538-3881/aafb36

Hue, V., Greathouse, T. K., Bonfond, B., Saur, J., Gladstone, G. R., Roth, L., et al. (2019). Juno-UVS observation of the Io footprint during solar eclipse. *Journal of Geophysical Research (Space Physics)*, *124*(7), 5184–5199. https://doi.org/10.1029/2018JA026431

Hue, V., Szalay, J. R., Greathouse, T. K., Bonfond, B., Kotsiaros, S., Louis, C. K., et al. (2022). A comprehensive set of Juno in situ and remote sensing observations of the Ganymede auroral footprint. *Geophysical Research Letters*, *49*(7), e96994. https://doi.org/10.1029/2021GL096994

Huscher, E., Bagenal, F., Wilson, R. J., Allegrini, F., Ebert, R. W., Valek, P. W., et al. (2021). Survey of Juno observations in Jupiter's plasma disk: Density. *Journal of Geophysical Research (Space Physics)*, *126*(8), e29446. https://doi.org/10.1029/2021JA029446

Jacobsen, S., Neubauer, F. M., Saur, J., & Schilling, N. (2007). Io's nonlinear MHD-wave field in the heterogeneous Jovian magnetosphere. *Geophysical Research Letters*, *34*(10), L10202. https://doi.org/10.1029/2006GL029187

Kammer, J. A., Hue, V., Greathouse, T. K., Gladstone, G. R., Davis, M. W., & Versteeg, M. H. (2019). Planning operations in Jupiter's high-radiation environment: Optimization strategies from Juno-ultraviolet spectrograph. *Journal of Astronomical Telescopes, Instruments, and Systems*, *5*(02), 027001. https://doi.org/10.1117/1.JATIS.5.2.027001

Krupp, N., Vasyliunas, V. M., Woch, J., Lagg, A., Khurana, K. K., Kivelson, M. G., et al. (2004). Dynamics of the Jovian magnetosphere. In F. Bagenal, T. E. Dowling, & W. B. McKinnon (Eds.), *Jupiter. The planet, satellites and magnetosphere* (Vol. 1, pp. 617–638).

Lamy, L., Colomban, L., Zarka, P., Prangé, R., Marques, M. S., Louis, C. K., et al. (2022). Determining the beaming of Io decametric emissions: A remote diagnostic to probe the Io-Jupiter interaction. *Journal of Geophysical Research (Space Physics)*, *127*(4), e30160. https://doi.org/10.1029/2021JA030160

Louarn, P., Allegrini, F., McComas, D. J., Valek, P. W., Kurth, W. S., André, N., et al. (2018). Observation of electron conics by Juno: Implications for radio generation and acceleration processes. *Geophysical Research Letters*, *45*(18), 9408–9416. https://doi.org/10.1029/2018GL078973

Louarn, P., Allegrini, F., McComas, D. J., Valek, P. W., Kurth, W. S., André, N., et al. (2017). Generation of the Jovian hectometric radiation. *First lessons from Juno*, *44*(10), 4439–4446. https://doi.org/10.1002/2017GL072923

Louis, C. K., Lamy, L., Zarka, P., Cecconi, B., Hess, S. L. G., & Bonnin, X. (2017). Simulating jupiter-satellite decametric emissions with ExPRES: A parametric study. In G. Fischer, G. Mann, M. Panchenko, & P. Zarka (Eds.), *Planetary radio emissions viii* (pp. 59–72). https://doi.org/10.1553/PRE8s59

Louis, C. K., Hess, S. L. G., Cecconi, B., Zarka, P., Lamy, L., Aicardi, S., & Loh, A. (2019). ExPRES: An exoplanetary and planetary radio emissions simulator. *A&A*, *627*, A30. https://doi.org/10.1051/0004-6361/201935161

Louis, C. K., Hess, S. L. G., Cecconi, B., Zarka, P., Lamy, L., Aicardi, S., & Loh, A. (2023). maserlib/expres: Version 1.2.0. *Zenodo*. (This work has also been supported by the EPN-2024-RI (Europlanet 2024 Research Infrastructure) project, under contract number 871149 with the EC.). https://doi.org/10.5281/zenodo.7759511

Louis, C. K., Lamy, L., Zarka, P., Cecconi, B., & Hess, S. L. G. (2017). Detection of Jupiter decametric emissions controlled by Europa and Ganymede with voyager/PRA and Cassini/RPWS. *Journal of Geophysical Research (Space Physics)*, *122*(9), 9228–9247. https://doi.org/10.1002/2016JA023779

Louis, C. K., Lamy, L., Zarka, P., Cecconi, B., Imai, M., Kurth, W. S., et al. (2017). Io-Jupiter decametric arcs observed by Juno/Waves compared to ExPRES simulations. *Geophysical Research Letters*, *44*(18), 9225–9232. https://doi.org/10.1002/2017GL073036

Louis, C. K., Louarn, P., Allegrini, F., Kurth, W. S., & Szalay, J. R. (2020). Ganymede-induced decametric radio emission: In situ observations and measurements by Juno. *Geophysical Research Letters*, *47*(20), e90021. https://doi.org/10.1029/2020GL090021

Louis, C. K., Zarka, P., Dabidin, K., Lampson, P. A., Magalhães, F. P., Boudouma, A., et al. (2021). Latitudinal beaming of Jupiter's radio emissions from Juno/waves flux density measurements. *Journal of Geophysical Research (Space Physics)*, *126*(10), e29435. https://doi.org/10.1029/2021JA029435

Markwardt, C. B. (2009). Non-linear least-squares fitting in IDL with MPFIT. In D. A. Bohlender, D. Durand, & P. Dowler (Eds.), *Astronomical data analysis software and systems xviii* (Vol. 411, p. 251).

Marques, M. S., Zarka, P., Echer, E., Ryabov, V. B., Alves, M. V., Denis, L., & Coffre, A. (2017). Statistical analysis of 26 yr of observations of decametric radio emissions from Jupiter. *A&A*, *604*, A17. https://doi.org/10.1051/0004-6361/201630025

Mura, A., Adriani, A., Connerney, J. E. P., Bolton, S., Altieri, F., Bagenal, F., et al. (2018). Juno observations of spot structures and a split tail in Io-induced aurorae on Jupiter. *Science*, *361*(6404), 774–777. https://doi.org/10.1126/science.aat1450

Neubauer, F. M. (1980). Nonlinear standing Alfven wave current system at Io-Theory. *Journal of Geophysical Research*, *85*(A3), 1171–1178. https://doi.org/10.1029/JA085iA03p01171

Prangé, R., Rego, D., Southwood, D., Zarka, P., Miller, S., & Ip, W. (1996). Rapid energy dissipation and variability of the lo-Jupiter electrodynamic circuit. *Nature*, *379*(6563), 323–325. https://doi.org/10.1038/379323a0

Promfu, T., Nichols, J. D., Wannawichian, S., Clarke, J. T., Vogt, M. F., & Bonfond, B. (2022). Ganymede's auroral footprint latitude: Comparison with magnetodisc model. *Journal of Geophysical Research (Space Physics)*, *127*(12), e2022JA030712. https://doi.org/10.1029/2022JA030712

Saur, J., Grambusch, T., Duling, S., Neubauer, F. M., & Simon, S. (2013). Magnetic energy fluxes in sub-Alfvénic planet star and moon planet interactions. *A&A*, *552*, A119. https://doi.org/10.1051/0004-6361/201118179

Steffl, A. J., Delamere, P. A., & Bagenal, F. (2006). Cassini UVIS observations of the Io plasma torus. III. Observations of temporal and azimuthal variability. *Icarus*, *180*(1), 124–140. https://doi.org/10.1016/j.icarus.2005.07.013

Su, Y.-J., Ergun, R. E., Bagenal, F., & Delamere, P. A. (2003). Io-related Jovian auroral arcs: Modeling parallel electric fields. *Journal of Geophysical Research (Space Physics)*, *108*(A2), 1094. https://doi.org/10.1029/2002JA009247

Sulaiman, A. H., Hospodarsky, G. B., Elliott, S. S., Kurth, W. S., Gurnett, D. A., Imai, M., et al. (2020). Wave-particle interactions associated with Io's auroral footprint: Evidence of Alfvén, ion cyclotron, and whistler modes. *Geophysical Research Letters*, *47*(22), e88432. https://doi.org/10.1029/2020GL088432

Sulaiman, A. H., Szalay, J. R., Clark, G., Allegrini, F., Bagenal, F., Brennan, M. J., et al. (2023). Poynting fluxes, field-aligned current densities, and the efficiency of the io-jupiter electrodynamic interaction. https://doi.org/10.22541/essoar.167768118.88908828/v1

Szalay, J. R., Allegrini, F., Bagenal, F., Bolton, S. J., Bonfond, B., Clark, G., et al. (2020a). *Alfvénic acceleration sustains Ganymede's footprint tail aurora*, *47*(3), e86527. https://doi.org/10.1029/2019GL086527

Szalay, J. R., Allegrini, F., Bagenal, F., Bolton, S. J., Bonfond, B., Clark, G., et al. (2020b). A new framework to explain changes in Io's footprint tail electron fluxes. *Geophysical Research Letters*, *47*(18), e89267. https://doi.org/10.1029/2020GL089267

Szalay, J. R., Bagenal, F., Allegrini, F., Bonfond, B., Clark, G., Connerney, J. E. P., et al. (2020). Proton acceleration by Io's Alfvénic interaction. *Journal of Geophysical Research (Space Physics)*, *125*(1), e27314. https://doi.org/10.1029/2019JA027314

Szalay, J. R., Bonfond, B., Allegrini, F., Bagenal, F., Bolton, S., Clark, G., et al. (2018). In situ observations connected to the Io footprint tail aurora. *Journal of Geophysical Research: Planets*, *123*(11), 3061–3077. https://doi.org/10.1029/2018JE005752

Thomas, N., Bagenal, F., Hill, T. W., & Wilson, J. K. (2004). The Io neutral clouds and plasma torus. In F. Bagenal, T. E. Dowling, & W. B. McKinnon (Eds.), *Jupiter. the planet, satellites and magnetosphere* (pp. 561–591).

Treumann, R. A. (2006). The electron-cyclotron maser for astrophysical application. *The Astronomy and Astrophysics Review*, *13*(4), 229–315. https://doi.org/10.1007/s00159-006-0001-y

Tsuchiya, F., Yoshioka, K., Kimura, T., Koga, R., Murakami, G., Yamazaki, A., et al. (2018). Enhancement of the Jovian magnetospheric plasma circulation caused by the change in plasma supply from the satellite Io. *Journal of Geophysical Research (Space Physics)*, *123*(8), 6514–6532. https://doi.org/10.1029/2018JA025316

Vogt, M. F., Bagenal, F., & Bolton, S. J. (2022). Magnetic field conditions upstream of Ganymede. *Journal of Geophysical Research (Space Physics)*, *127*(12), e2022JA030497. https://doi.org/10.1029/2022JA030497

Vogt, M. F., Rutala, M., Bonfond, B., Clarke, J. T., Moore, L., & Nichols, J. D. (2022). Variability of Jupiter's main auroral emission and satellite footprints observed with hst during the galileo era. *Journal of Geophysical Research: Space Physics*, *127*(2), e2021JA030011. https://doi.org/10.1029/2021JA030011

Wannawichian, S., Clarke, J. T., Bagenal, F., Smyth, W. H., Peterson, C. A., & Nichols, J. D. (2013). Longitudinal modulation of the brightness of Io's auroral footprint emission: Comparison with models. *Journal of Geophysical Research (Space Physics)*, *118*(6), 3336–3345. https://doi.org/10.1002/jgra.50346

Wu, C. S. (1985). Kinetic cyclotron and synchrotron maser instabilities: Radio emission processes by direct amplification of radiation. *Space Science Reviews*, *41*(3–4), 215–298. https://doi.org/10.1007/BF00190653

Wu, C. S., & Lee, L. C. (1979). A theory of the terrestrial kilometric radiation. *The Astrophysical Journal*, *230*, 621–626. https://doi.org/10.1086/157120

Yoneda, M., Kagitani, M., Tsuchiya, F., Sakanoi, T., & Okano, S. (2015). Brightening event seen in observations of Jupiter's extended sodium nebula. *Icarus*, *261*, 31–33. https://doi.org/10.1016/j.icarus.2015.07.037

Yoshikawa, I., Suzuki, F., Hikida, R., Yoshioka, K., Murakami, G., Tsuchiya, F., et al. (2017). Volcanic activity on Io and its influence on the dynamics of the Jovian magnetosphere observed by EXCEED/Hisaki in 2015. *Earth Planets and Space*, *69*(1), 110. https://doi.org/10.1186/s40623-017-0700-9

Yoshikawa, I., Yoshioka, K., Murakami, G., Yamazaki, A., Tsuchiya, F., Kagitani, M., et al. (2014). Extreme ultraviolet radiation measurement for planetary atmospheres/magnetospheres from the Earth-orbiting spacecraft (extreme ultraviolet spectroscope for exospheric dynamics: EXCEED). *Space Science Reviews*, *184*(1–4), 237–258. https://doi.org/10.1007/s11214-014-0077-z